



Enhancing the low-temperature CO₂ methanation over Ni/La-CeO₂ catalyst: The effects of surface oxygen vacancy and basic site on the catalytic performance

Tengfei Zhang^{a,b,1}, Weiwei Wang^{c,1}, Fangna Gu^{b,*}, Wenqing Xu^{b,*}, Jianling Zhang^b, Zhenxing Li^{c,*}, Tingyu Zhu^b, Guangwen Xu^{d,e}, Ziyi Zhong^{f,g}, Fabing Su^{b,e,**}

^a School of Chemical Engineering, University of Chinese Academy of Sciences, Beijing 100049, China

^b State Key Laboratory of Multiphase Complex Systems, Institute of Process Engineering, Chinese Academy of Sciences, Beijing 100190, China

^c State Key Laboratory of Heavy Oil Processing, China University of Petroleum, Beijing 102249, China

^d Key Laboratory on Resources Chemicals and Materials of Ministry of Education, Shenyang University of Chemical Technology, Shenyang 110142, China

^e Institute of Industrial Chemistry and Energy Technology, Shenyang University of Chemical Technology, Shenyang 110142, China

^f Department of Chemical Engineering, Guangdong Technion Israel Institute of Technology (GTIIT), 241 Daxue Road, Shantou 515063, China

^g Technion Israel Institute of Technology (IIT), Haifa 32000, Israel

ARTICLE INFO

Keywords:

CO₂ methanation

Ni catalyst

La-Ce-O solid solution

Performance

Mechanism

ABSTRACT

This work reports a strategy to promote the low-temperature CO₂ methanation on the Ni-based catalyst by tuning the surface oxygen vacancy and medium-strength basic sites of the CeO₂ support and thus changing the reaction pathway. La species was introduced into CeO₂ support and calcined at 600 °C (CeO₂-La-600) to form a La-Ce-O solid solution with a thin La₂O₃ layer on the surface, generating more basic sites and oxygen vacancies. This unique structure facilitated the adsorption and direct dissociation of CO₂. Over Ni/CeO₂-La-600, the reaction follows the HCOO* and *CO pathways, while over Ni/CeO₂-600, the reaction occurs via the HCOO* pathway only. The decomposition of CO₂ * to *CO is energetically more favorable than hydrogenation to HCOO* on Ni/CeO₂-La-600, resulting in its higher catalytic performance at low temperatures. This work unravels the complex interplay among oxygen vacancy, basic site, and reaction pathway in CO₂ methanation over the Ni-based catalysts.

1. Introduction

Capturing carbon dioxide (CO₂) and reacting it with renewable H₂ is one of the strategies to reduce CO₂ emission and valorize it. This approach can produce a wide variety of high-value chemicals and feedstocks, including methane, ethanol, methanol, and higher hydrocarbons [1]. Among these reactions, the CO₂ methanation reaction is regarded as a promising process for recycling and utilizing CO₂ and implementing the power-to-gas technology, which has great potential for commercial applications and environmental benefits [2,3]. This reaction (CO₂ + 4 H₂ ↔ CH₄ + 2 H₂O, ΔH_{298 K} = −165 kJ mol^{−1}) should be run at relatively high temperatures in terms of its kinetics. However, it is also a highly exothermic reaction favoring low reaction temperatures to

reduce the formation of byproducts [4] and, in some cases, to avoid the sintering of the active component particles in catalysts [4]. Supported Ni catalysts are often employed in CO₂ methanation due to their relatively high catalytic performance and low cost [5–7]. However, these Ni-based catalysts often suffer from poor activity at low temperatures less than 300 °C, especially in activating the chemically inert CO₂ molecules to CH₄ [8]. Great efforts thus have been made in catalyst synthesis to improve the dispersion of Ni particles to increase the available active sites [9,10].

The performance of a Ni-based catalyst is usually related to its support property. In recent decades, many supports have been employed in Ni catalysts for CO₂ methanation, including Al₂O₃ [11], SiO₂ [12], TiO₂ [13], CeO₂ [14], MgO [15], CNTs [16], zeolite [17] and ZrO₂ [18].

* Corresponding authors.

** Corresponding author at: State Key Laboratory of Multiphase Complex Systems, Institute of Process Engineering, Chinese Academy of Sciences, Beijing 100190, China.

E-mail addresses: fngu@ipe.ac.cn (F. Gu), wqxu@ipe.ac.cn (W. Xu), lizzx@cup.edu.cn (Z. Li), fbsu@ipe.ac.cn (F. Su).

¹ Tengfei Zhang and Weiwei Wang contributed equally to this work.

Among them, CeO_2 support is a good candidate because of its abundant surface oxygen vacancies [19]. For example, Li et al. reported the presence of a strong metal-oxide interaction between the supported hexagonal Ni nanocrystallites and CeO_2 in a Ni/ CeO_2 catalyst, which selectively produced CH_4 with higher turnover frequencies (TOFs) than that over the Ni nanoparticles supported on TiO_2 and SiO_2 [20]. Tang et al. reported the Ni/ CeO_2 catalysts derived from Ce-MOF precursor for CO_2 methanation, which showed superior activity since Ni could be partially incorporated into ceria lattice, leading to the formation of $\text{Ce}_{1-x}\text{Ni}_x\text{O}_{2-y}$ solid solutions and oxygen vacancies [21]. Feng et al. synthesized a Ni/ CeO_2 catalyst with a novel structure by impregnating a Ce-based metal-organic framework (MOF) compound with a Ni precursor, showing a very high CO_2 conversion and good CH_4 selectivity [22].

CeO_2 support with different morphologies and structures, such as nanoplates [23], nanorods [24,25], nanocubes [26], nanoflowers [27], and nanowires [27], have been used as Ni catalyst supports. Although many synthesis methods for CeO_2 supports have been investigated, including precipitation [28], microwave [29], hydrothermal [21], and evaporation [29], hydrothermal synthesis is widely used to prepare nanostructured CeO_2 because it can rationally alter the morphology of CeO_2 to obtain various structures [30]. Three-dimensional (3D) hierarchical and mesoporous CeO_2 with a high surface area has advantages for both catalyst and catalyst support applications, because this kind of structure can effectively facilitate the dispersion of active components and enhance the transportation of reactant molecules to the active sites [31].

To improve the stability and reactivity of the CeO_2 supports, researchers have tried to introduce some other metal ions into CeO_2 to form solid solutions. It is reported that incorporating La_2O_3 into CeO_2 could form a solid solution and facilitate the generation of oxygen defects [32]. Reddy and coworkers showed that doping La species greatly increased the oxygen storage/release capacity of CeO_2 because the substitution of Ce^{4+} cations with La^{3+} cations needs more oxygen vacancies with La^{3+} cations to maintain charge neutrality [33]. Xiao and co-authors reported that La-doped ceria supported Ni (Ni-CeLa_{0.20}) exhibited superior catalytic performance in the steam reforming of ethanol, which is ascribed to its large abundant oxygen vacancies and suitable metal-supported interaction [34]. On the other hand, La is usually used as a promoter to improve the catalytic properties of Ni catalysts in methanation reaction because La species can effectively restrain the growth of active Ni nanoparticles and improve the dispersion of Ni particles. It has been reported that La-promoted Ni/MgAl₂O₄ [35], La-promoted Ni/Al₂O₃ [36], La-promoted Ni/Na-BETA [37], La-promoted NiAl-LDH/Ni-foam [38], La-modified Ni/SBA-15 [39], La_2O_3 -modified Ni/MFI nanosponge [40], La_2O_3 -modified Ni/ CeO_2 [41], La-promoted Ni/ SiO_2 [42], La-promoted Ni/SiC [43], and La-promoted Ni/ SiO_2 - γ -Al₂O₃ [44] catalysts could enhance the low-temperature methanation activity. In addition, Wang and coauthors found that Ni/ La_2O_3 catalysts with metal-carbonate interfaces exhibited superior activity and higher anti-CO poisoning stability than Ni/ La_2O_3 catalysts in CO_2 methanation [45]. However, the function of doped La species in these Ni-based catalysts is not very clear.

Mainly two reaction mechanisms for CO_2 methanation have been reported, depending on the surface property of the Ni-based catalysts [19]. They are: (1) the $^*\text{CO}$ pathway, via the activation of CO_2 into $^*\text{CO}$ that further reacts with $^*\text{H}$ to form CH_4 , and (2) the HCOO^* pathway, via hydrogenation of adsorbed CO_2 species into HCOO^* and further stepwise hydrogenation to CH_4 . It is found that the reaction on the Ni catalyst surface with abundant basic sites follows the $^*\text{CO}$ pathway, but the HCOO^* pathway occurs in the absence of basic sites [46]. CO_2 methanation via the $^*\text{CO}$ pathway requires a lower activation energy and lower temperature than the HCOO^* pathway [47]. Therefore, creating more basic sites and oxygen vacancies on CeO_2 support should be essential to boost the low-temperature catalytic performance of Ni/ CeO_2 catalyst in CO_2 methanation by altering the reaction pathway.

In this work, we chose flower-like hollow CeO_2 microspheres with and without La doping as the model Ni-based catalyst supports to investigate the effects of surface oxygen vacancy and basic site on the catalytic performance in low-temperature CO_2 methanation. We synthesized CeO_2 -600, CeO_2 -La-600, and CeO_2 -La-800 microsphere supports via a hydrothermal method followed by calcination at 600, 600, and 800 °C, respectively. Ni/ CeO_2 -600, Ni/ CeO_2 -La-600, and Ni/ CeO_2 -La-800 catalysts with a Ni loading of 10 wt% were further prepared by the impregnation method followed by H_2 reduction. It is found that a La-Ce-O solid solution was formed in CeO_2 -La-600 and CeO_2 -La-800 supports. Compared to Ni/ CeO_2 -600, both Ni/ CeO_2 -La-600 and Ni/ CeO_2 -La-800 possess more surface oxygen vacancies, and Ni/ CeO_2 -La-600 has more basic sites due to the generation of $\text{La}_2\text{O}_3\text{CO}_3$ on the surface of the La-Ce-O solid solution. Ni/ CeO_2 -La-600 showed higher catalytic performance than Ni/ CeO_2 -La-800 and Ni/ CeO_2 -600 in the low-temperature CO_2 methanation. In situ DRIFTS and calculations confirm that the reaction route on the Ni/ CeO_2 -La-600 catalyst with more surface oxygen vacancies and basic sites follows both HCOO^* and $^*\text{CO}$ pathways, but the reaction route on Ni/ CeO_2 -600 without surface oxygen vacancies and basic sites only follows HCOO^* pathway. This work provides a new theoretical understanding of CO_2 activation and methanation mechanism and a practical way to enhance the low-temperature CO_2 methanation activity of Ni-based catalysts.

2. Experimental section

2.1. Chemicals and materials

Glucose was purchased from Sigma-Aldrich Co., USA, and acrylamide from Adamas Reagent, Ltd., China. All the other chemicals of analytical grade, including nickel nitrate hexahydrate ($\text{Ni}(\text{NO}_3)_2 \cdot 6\text{H}_2\text{O}$, purity > 98%), cerium nitrate hexahydrate ($\text{Ce}(\text{NO}_3)_3 \cdot 6\text{H}_2\text{O}$, purity > 99%), ethylene glycol ($(\text{CH}_2\text{OH})_2$, purity > 99.8%) and lanthanum nitrate hexahydrate ($\text{La}(\text{NO}_3)_3 \cdot 6\text{H}_2\text{O}$, purity > 99%), were purchased from Shanghai Macklin Biochemical Co., Ltd., China, and were used without further treatment.

2.2. Synthesis of materials

2.2.1. Synthesis of supports

The CeO_2 support was prepared using a hydrothermal method [30]. Glucose (0.01 mol) and acrylamide (0.015 mol) were dissolved in deionized water (80 mL) under stirring, followed by the addition of a stoichiometric amount of $\text{Ce}(\text{NO}_3)_3 \cdot 6\text{H}_2\text{O}$ (0.005 mol) to form a transparent solution. Then, 3.2 mL of 25 wt% ammonia solution was added dropwise under stirring. The pH value of the resultant mixture remained at approximately 10. This mixture was stirred for 5 h before being transferred into a 100 mL Teflon-lined autoclave. The autoclave was kept at 180 °C for 72 h and cooled to room temperature naturally; the solid precipitate was collected by filtration and washed with deionized water and alcohol four times. Finally, it was dried at 100 °C for 10 h and calcined at 600 °C for 2 h in air at a heating rate of 5 °C min⁻¹. The collected samples were denoted as CeO_2 -600.

The La-doped CeO_2 support was prepared by similar procedures, but aqueous ammonia solution was added dropwise into a mixed solution of 0.216 g $\text{La}(\text{NO}_3)_3 \cdot 6\text{H}_2\text{O}$ and 1.95 g $\text{Ce}(\text{NO}_3)_3 \cdot 6\text{H}_2\text{O}$ with a La/Ce molar ratio of 1:9. The obtained precipitate was calcined at 600 and 800 °C for 2 h in air at a heating rate of 5 °C min⁻¹. The collected samples were denoted as CeO_2 -La-600 and CeO_2 -La-800, respectively.

2.2.2. Synthesis of supported Ni catalysts

Ni was loaded onto the support by the incipient wetness impregnation method. $\text{Ni}(\text{NO}_3)_2 \cdot 6\text{H}_2\text{O}$ (0.165 g) was dissolved in a certain amount of ethylene glycol (0.2 mL), and then, the above solution was added dropwise to fresh support powder (0.3 g), sealed at 40 °C for 24 h, dried at 100 °C for 12 h, and calcined at 400 °C for 2 h in air at a heating

rate of 5 °C min⁻¹. The collected products were denoted as NiO/CeO₂-600, NiO/CeO₂-La-600, and NiO/CeO₂-La-800, which were further reduced in H₂ gas at 400 °C for 1 h (heating rate of 5 °C min⁻¹, H₂ flow rate of 50 mL min⁻¹) and denoted as Ni/CeO₂-600, Ni/CeO₂-La-600, and Ni/CeO₂-La-800 with a Ni loading of 10 wt%, respectively.

2.3. Characterization

The samples were characterized by various techniques, including nitrogen adsorption, X-ray diffraction (XRD), scanning electron microscopy (SEM), transmission electron microscopy (TEM), high-angle annular dark-field scanning transmission electron microscopy (HAADF-STEM), H₂ temperature-programmed reduction (H₂-TPR), H₂ temperature-programmed desorption (H₂-TPD), CO₂ temperature-programmed desorption (CO₂-TPD), X-ray photoelectron spectroscopy (XPS), Raman spectra, Fourier-transform infrared spectra (FT-IR) and in situ diffuse reflectance infrared Fourier transform spectroscopy (in situ DRIFTS). The detailed operation procedures of the above characterizations can be found in [Supporting Information](#).

2.4. Catalytic measurement

The catalytic activity test was carried out in a fixed bed reactor by placing the catalyst in a quartz tube (I.D. 8 mm) at 0.1 MPa, in which the thermocouple was inserted into the furnace chamber to control the reaction temperature. A small amount of the catalyst was used with quartz wools packed on the top of the catalyst bed as the gas distributor to avoid the influence of mass transfer. Additionally, the catalyst bed (catalyst diluted with quartz sand, ca. 6 cm) was positioned in the flat-temperature zone (ca. 10 cm) of the furnace to avoid the influence of heat transfer, and the addition of the quartz sands was to avoid the generation of hotspots in the catalyst bed. Moreover, another thermocouple was inserted into the catalyst bed with a casing pipe to measure its temperature. Combined with the above strategies, the influence of mass and heat transfers were eliminated before the catalytic tests. For the activity test, typically, 0.1 g catalyst (20–40 mesh) diluted with 5.0 g quartz sand (20–40 mesh) was uploaded to a quartz tube with a height of ca. 6 cm, and the gas flow rate was 50 mL min⁻¹, corresponding to a weight hourly space velocity of 30000 mL g⁻¹ h⁻¹. First, the catalyst was reduced at 400 °C in pure H₂ (100 mL min⁻¹) for 1 h and then cooled to the starting reaction temperature in H₂. Then, the mixed CO₂ and H₂ as well as N₂ (as an internal standard) were introduced into the reactor at a molar ratio of CO₂/H₂/N₂ = 9/36/5 (100 mL min⁻¹) to investigate the catalytic activity of Ni-based catalysts at 250–400 °C. The temperature-programmed heating rate was 5 °C min⁻¹ in the total temperature range, and to reach and maintain the steady state, it was kept for 1 h at each temperature point before the product analysis. Inlet and outlet gases were analyzed online by a Micro GC 3000 A (Fusion, INFICON) equipped with a TCD. In addition, a 100 h lifetime test of CO₂ methanation was performed at 325 °C, 0.1 MPa, 30000 mL g⁻¹ h⁻¹. The CO₂ conversion, CH₄ selectivity and CH₄ yield are defined as follows [8]:

$$\text{CO}_2 \text{ conversion : } X_{\text{CO}_2} = \frac{V_{\text{CO}_2, \text{in}} - V_{\text{CO}_2, \text{out}}}{V_{\text{CO}_2, \text{in}}} \times 100\% \quad (1)$$

$$\text{CH}_4 \text{ selectivity : } S_{\text{CH}_4} = \frac{V_{\text{CH}_4, \text{out}}}{V_{\text{CO}_2, \text{in}} - V_{\text{CO}_2, \text{out}}} \times 100\% \quad (2)$$

$$\text{CH}_4 \text{ yield : } Y_{\text{CH}_4} = \frac{V_{\text{CH}_4, \text{out}}}{V_{\text{CO}_2, \text{in}}} \times 100\% \quad (3)$$

where X is the conversion of CO₂, S is the selectivity of CH₄, Y is the CH₄ yield, V_{CO₂,in} and V_{CO₂,out} are the volume flow rates of CO₂ at the inlet and outlet of the reactor at standard temperature and pressure (STP), mL min⁻¹.

The normalized rate and activation energy for CO₂ methanation over

the catalysts were measured at 0.1 MPa with 0.2 g (20–40 mesh) catalyst diluted with 5.0 g quartz sand (20–40 mesh). The experiments were performed at different total gas flow rates of 50, 100, and 200 mL min⁻¹ at temperatures of 180, 190, 200 and 210 °C to maintain a CO₂ conversion in the range of 5–10%. The rate (R_w) was determined using the following equation [8]:

$$\text{Rate}(r) = \frac{F_{\text{CO}_2} \times X_{\text{CO}_2}}{W} = \frac{X_{\text{CO}_2}}{W/F_{\text{CO}_2}} \quad (4)$$

where F_{CO₂} represents the flow of CO₂ in mol min⁻¹, W is the weight of the catalyst in g, and X_{CO₂} is the CO₂ conversion. The variations in X_{CO₂} with respect to W/F_{CO₂} were plotted, and then the reaction rates were calculated at various temperatures from the slope of the linear portion (The "linear portion" means a straight line fitted by three points (Fig. S3)). Finally, the graph was plotted with ln(rate) as the vertical coordinate and temperature as the horizontal coordinate. The activation energy was calculated using the Arrhenius equation.

The effects of particle size and linear speed on diffusional limitation over the Ni/CeO₂-La-600 were measured at 0.1 MPa with 0.2 g (10–20, 20–40, and 40–60 mesh) catalyst. The experiments were performed at different molar flow rates (mol/h).

2.5. Computational detail

All spin-polarized calculations were performed using the Vienna ab initio Simulation Package (VASP). The Perdew–Burke–Ernzerhof (PBE) parametrization of the generalized gradient approximation (GGA) was used to describe the electronic exchange-correlation energies. The criterion of total energy convergence in the optimization of the atomic structure is 10⁻⁵ eV, the convergence criterion of the atomic force is 0.05 eV/Å, and the cut-off energy of plane wave expansion is 400 eV. The Brillouin zone was sampled using the Monkhorst–Pack method with 2 × 2 × 1 k-point meshes. A vacuum layer of 15 Å was used along the c direction normal to the surface to avoid periodic interaction. The bottom atoms with fractional coordinates of < 0.2 were fixed, and the upper atoms were allowed to relax during the geometry optimization.

Ni₁₀/CeO_{2-x} was constructed with a Ni₁₀ cluster supported on the CeO_{2-x} (111) surface. The CeO₂ (111) slab was modeled using a (3 × 3) supercell. Afterward, the Ni₁₀ cluster was deposited on the CeO₂ (111) slab with one oxygen vacancy. On the other hand, the Ni₁₀/CeO_{2-x}-La model was constructed by replacing one Ce atom with a La atom on the surface of Ni₁₀/CeO_{2-x}. The La doping concentration is 3.7%.

3. Results and discussion

3.1. Characterization of the catalysts

3.1.1. SEM observation

Fig. 1 shows the SEM images of the three supports and the corresponding supported catalysts. CeO₂-600 has a flower-like microspherical morphology with a diameter of approximately 2–3 μm. Each microsphere consists of many nanosheets with thicknesses of 40–60 nm (Fig. 1a). After introducing La species, the flower-like structure is still maintained for CeO₂-La-600 (Fig. 1b) and CeO₂-La-800 (Fig. 1c). These 3D structures with a high surface area should be able to facilitate the dispersion of active nanoparticles and the effective transportation of reactant molecules [31]. With further loading of the Ni active species, Ni/CeO₂-600 (Fig. 1d), Ni/CeO₂-La-600 (Fig. 1e), and Ni/CeO₂-La-800 (Fig. 1f) still have the microspherical morphologies similar to that of CeO₂-600 (Fig. 1a), and there is no observation of obvious Ni particles, possibly because they were too small in size. Furthermore, the SEM elemental mapping images of Ni/CeO₂-La-600 (Fig. 1g and h) show the high dispersion of Ce (Fig. 1i), La (Fig. 1j), Ni (Fig. 1k), and O (Fig. 1l).

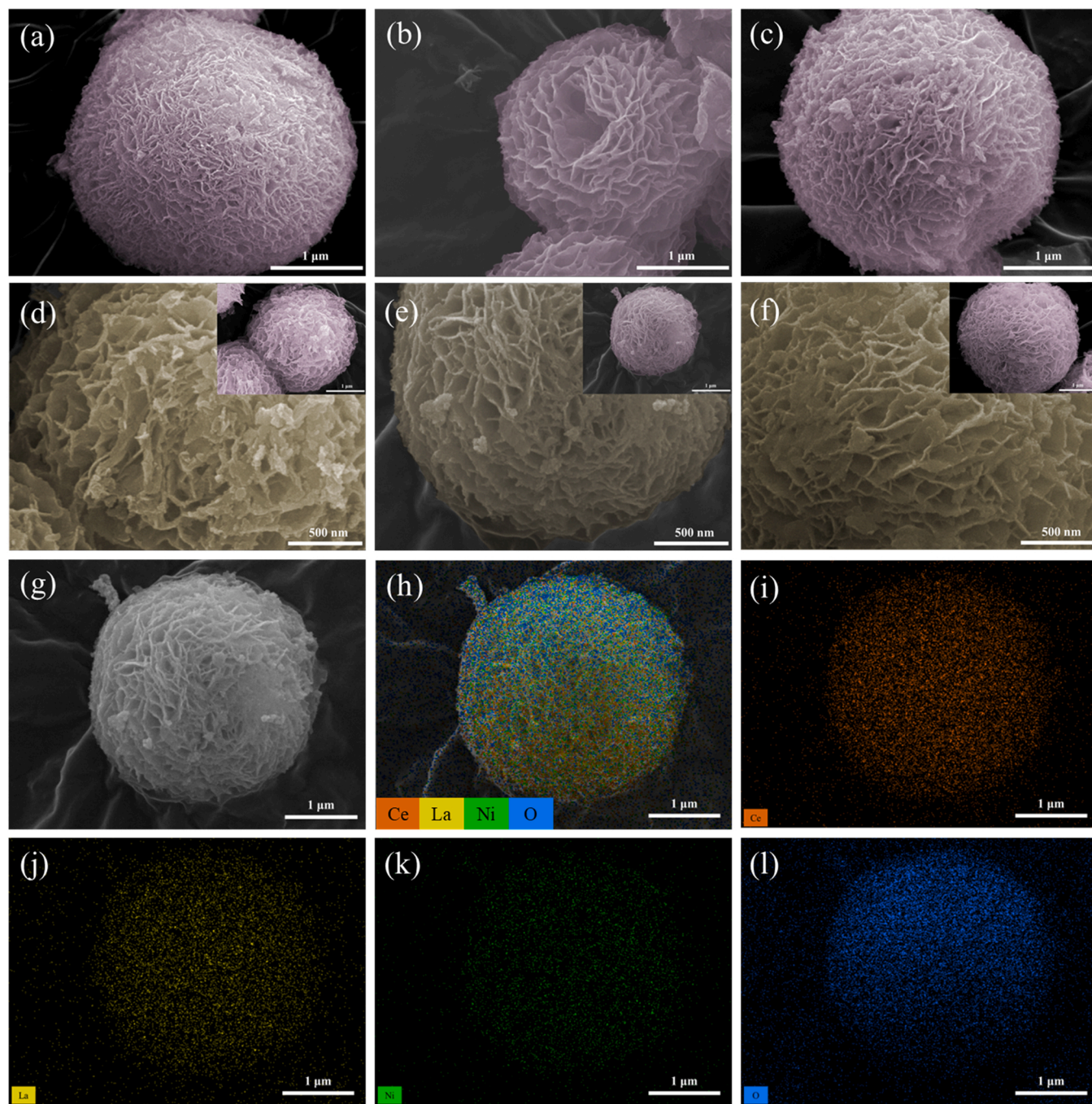


Fig. 1. SEM images: (a) CeO₂-600, (b) CeO₂-La-600, (c) CeO₂-La-800, (d) Ni/CeO₂-600, (e) Ni/CeO₂-La-600, and (f) Ni/CeO₂-La-800; SEM image (g), EDS element layered image (h) and elemental mapping images of Ce (i), La (j), Ni (k), and O (l) for Ni/CeO₂-La-600.

3.1.2. TEM observation

The TEM image of Ni/CeO₂-600 in Fig. 2a confirms the flower-like microspherical and hollow structure with approximately 2 μm in diameter. However, the small difference in contrast between Ni and CeO₂ makes it difficult to identify the Ni nanoparticles [48]. In the HRTEM image of Ni/CeO₂-600 (Fig. 2b), the observed interplanar spacings of 0.312, 0.270, and 0.190 nm correspond to the (111), (200), and (220) diffraction facets of CeO₂, respectively. For the TEM image of Ni/CeO₂-La-600, there is no obvious change after adding the La species (Fig. 2c). In the HRTEM image of Fig. 2d, the interplanar spacing of approximate 0.320 nm belongs to the (010) plane of La₂O₂CO₃ [49], while those of 0.315, 0.272, and 0.191 nm belong to CeO₂ (111), (200), and (220) respectively in Ni/CeO₂-La-600. The latter are slightly larger

than those in Ni/CeO₂-600, implying the formation of La-Ce-O solid solution and La₂O₂CO₃ in Ni/CeO₂-La-600 [19,50]. Fig. 2e-i display the elemental mapping images of Ce (Fig. 2f), La (Fig. 2g), O (Fig. 2h), and Ni (Fig. 2i), indicating that Ni is highly dispersed in CeO₂-La-600.

3.1.3. XRD and FT-IR analysis

Fig. 3a shows the XRD patterns of all the catalysts. For Ni/CeO₂-600, three strongest peaks are observed at 2θ values of 28.54, 47.48, and 56.34°, corresponding to the diffractions of the (111), (220), and (311) facets of CeO₂ with a cubic fluorite structure (JCPDS file no. 34-0394) [51,52]. For Ni/CeO₂-La-600, only the CeO₂ phase is detected, and there is no detection of any La-related species. Meanwhile, the 2θ value of the strongest (111) peak is slightly decreased compared with that of

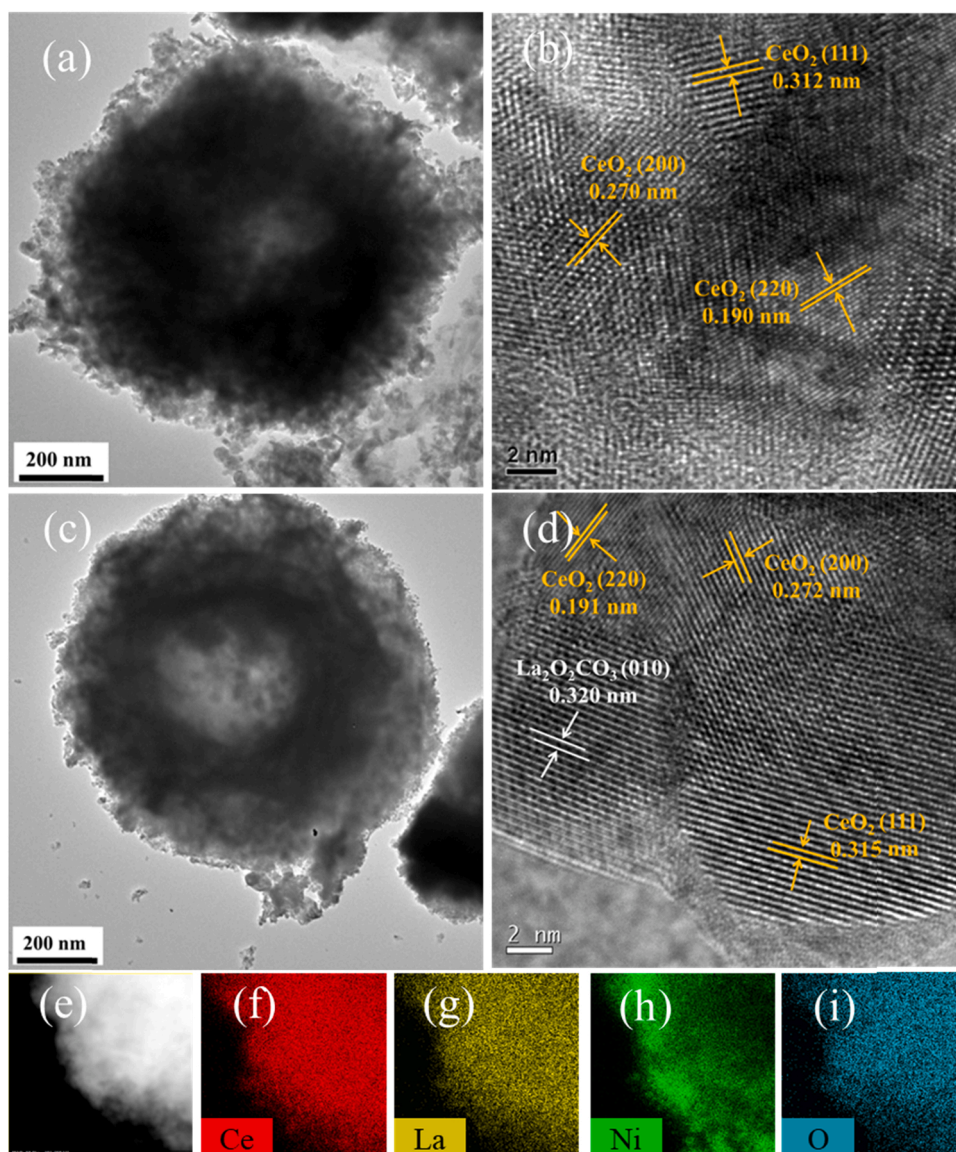


Fig. 2. TEM or HRTEM images: (a and b) Ni/CeO₂-600, (c and d) Ni/CeO₂-La-600, HAADF-STEM image (e) and corresponding elemental mappings images of Ce (f), La (g), Ni (h), and O (i) of Ni/CeO₂-La-600.

Ni/CeO₂-600 (Fig. 3b), and the unit cell side length increased from 5.407 to 5.433 Å (Table 1) probably because part of the La³⁺ ions confirmed by XPS was doped into CeO₂ to form a La-Ce-O solid solution and part was emerged from the La-Ce-O solid solution at the calcination temperature of 600 °C to generate La₂O₂CO₃ (Fig. S1). It has been reported that Ce⁴⁺ cations in CeO₂ with the cubic fluorite structure have a coordination number (CN) of 8 and an ionic radius of 0.87 Å. When La³⁺ cations are doped into the CeO₂ lattice to replace the corresponding amount of Ce⁴⁺ cations, its lattice side lengths will increase and the 2θ values decrease significantly, as the ionic radius of La³⁺ cations (1.03 Å) is much larger than that of Ce⁴⁺ cations [53]. In addition, the 2θ value of Ni/CeO₂-La-800 is slightly decreased compared to that of Ni/CeO₂-La-600 (Fig. 3b), probably because all the La³⁺ cations were doped into the CeO₂ lattice to form a solid solution structure. As proven, La₂O₂CO₃ began to decompose into La₂O₃ above 600 °C (Fig. S1) [54], and thus, there is no La₂O₂CO₃ on CeO₂-La-800. As shown in Fig. 3c, there is the observance of the FTIR peaks at 1383 and 852 cm⁻¹ for all the catalysts, corresponding to carbonate vibrations [55], and the Ni/CeO₂-La-600 catalyst has the strongest signal at 1383 cm⁻¹, implying the presence of more carbonate species. For all the catalysts, the

diffraction peak at 44.6° is attributed to the (111) plane of metallic Ni (JCPDS No. 01-070-1849) (Fig. 3d) [56–58]. The Ni crystal sizes of Ni/CeO₂-600, Ni/CeO₂-La-600, and Ni/CeO₂-La-800 are calculated by the Debye-Scherrer equation to be 8.4, 6.4, and 7.5 nm (Table 1), respectively, indicating that the incorporation of La species can reduce the Ni crystal size, resulting in higher dispersion [43,59].

3.1.4. N₂ adsorption isotherm analysis

Fig. 4 displays the nitrogen adsorption–desorption isotherms and pore size distribution (PSD) curves of all the catalysts. The type-IV curves with steep H4 hysteresis loops at high relative pressures (P/P_0) (Fig. 4a) are observed, indicating the formation of a mesoporous structure [31]. Their PSD curves in Fig. 4b show a narrow peak centered at 4.3 nm, implying the formation of mesoporous channels. All the catalysts have similar specific surface areas and pore volumes (Table 1). Notably, although the surface areas of all the catalysts decreased after loading Ni species, their adsorption–desorption isotherms, pore volumes, and PSD curves remained similar to those of their corresponding supports (Fig. S2 and Table S1), suggesting that these catalysts retained the pore structure of their supports.

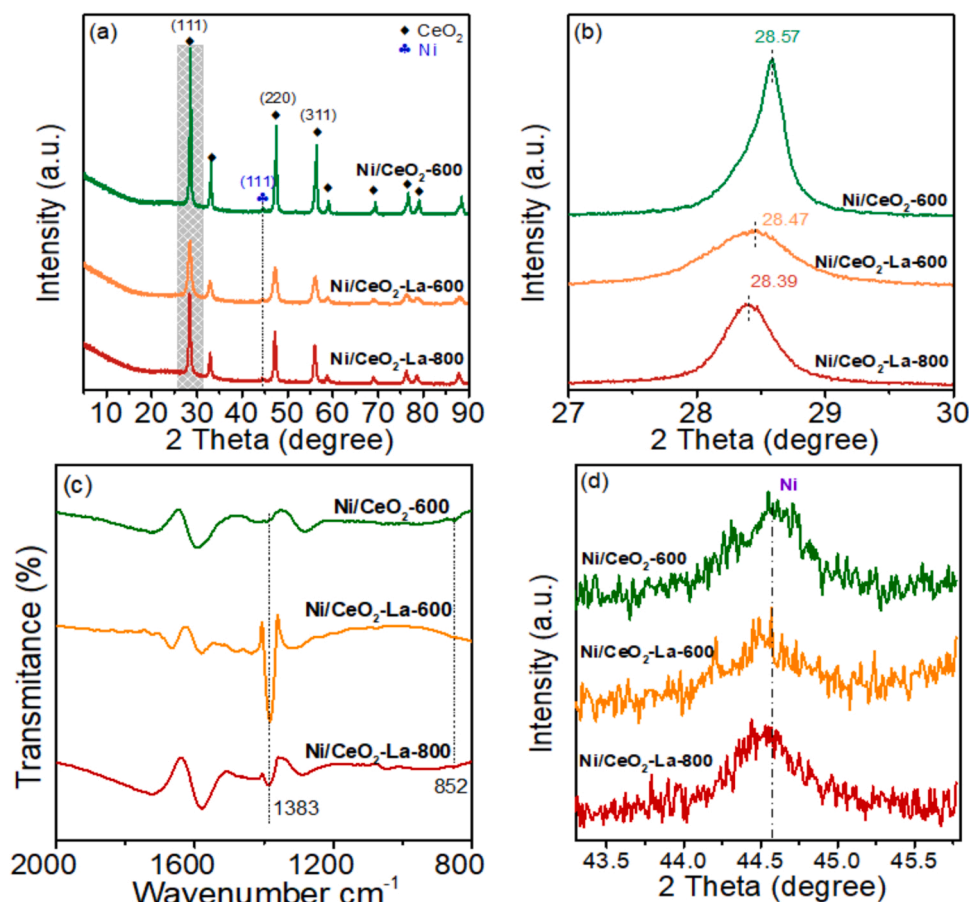


Fig. 3. (a) XRD patterns, (b) partially enlarged profiles of 27–30° in (a), (c) FT-IR spectra of all the catalysts, and (d) partially enlarged profiles of 43–46° in (a).

Table 1

Physical and chemical properties of the samples.

Samples	unit cell side length ^a (Å)	S _{BET} ^b (m ² g ⁻¹)	V _p ^c (cm ³ g ⁻¹)	Ni crystal Size ^d (nm)
Ni/CeO ₂ -600	5.407	65	0.10	8.4
Ni/CeO ₂ -La-600	5.433	60	0.13	6.4
Ni/CeO ₂ -La-800	5.441	57	0.11	7.5

^a XRD results for the CeO₂ phase in the samples, calculated by the Bragg equation ;

^b Surface area, derived from BET equation;

^c Pore volume, obtained from the volume of nitrogen adsorbed at a relative pressure of 0.99.

^d Ni crystal size, calculated by the XRD diffraction peak ($2\theta = 44.6$) using the Debye-Scherrer equation.

3.1.5. H₂-TPR, H₂-TPD, and CO₂-TPD analysis

Fig. 5a shows the H₂-TPR curves of NiO/CeO₂-600, NiO/CeO₂-La-600, and NiO/CeO₂-La-800. The observed strong peak at 335 °C and the weak peak at 219 °C can be ascribed to the strongly interacted NiO particles with the support and the reactive surface oxygen, respectively [27]. According to the H₂-TPR results, the reduction temperature was determined to be 400 °C, at which most of the NiO species could be reduced. For NiO/CeO₂-La-600, in addition to the above two reduction peaks, a new shoulder peak appears at 262 °C, suggesting the presence of a moderately interacted Ni species with the CeO₂-La-600 support [45]. The H₂ consumption of the NiO/CeO₂-600, NiO/CeO₂-La-600, and NiO/CeO₂-La-800 catalysts is also calculated to be 7.26, 11.85, and 9.20 mmol g⁻¹ (Table 2), respectively, indicating that doping La into

CeO₂ can improve the reducibility of NiO, consistent with a previous report [35,60]. It should be noted that the presence of La₂O₂CO₃ in NiO/CeO₂-La-600 may act as a fence to prevent the development of strong interaction between the NiO and the CeO₂-La-600 support, thus promoting H₂ consumption and the reducibility of NiO. In addition, we calculated the ideal amount of H₂ consumed on Ni/CeO₂-600, Ni/CeO₂-La-600, and Ni/CeO₂-La-800 by assuming that the Ni²⁺ ions in Ni/CeO₂-600, Ni/CeO₂-La-600, and Ni/CeO₂-La-800 were completely reduced to metallic Ni. The amount is much smaller than the H₂ consumption derived from the H₂-TPR peak. Possibly, this is because the partial reduction of the CeO₂ support and the spillover of H atoms overlap with the metal reduction peaks [61–64].

Fig. 5b shows the H₂-TPD of all the catalysts. Overall, these catalysts show only one hydrogen desorption peak in the temperature range of 100–250 °C, attributed to the chemisorbed hydrogen on the highly dispersed Ni nanoparticles. The integral area of this peak follows the order of Ni/CeO₂-600 < Ni/CeO₂-La-800 < Ni/CeO₂-La-600, indicating that Ni/CeO₂-La-600 has the largest number of active or defect sites that can serve as a capture center for surface hydrogen, thereby reducing the activation energy of H₂ dissociation [65]. Furthermore, the Ni dispersion in these catalysts is calculated based on the results of H₂-TPD and H₂-TPR (see Table 2). Among them, Ni/CeO₂-La-600 shows the highest Ni dispersion of 28.52% and H₂ uptake of 200.5 μmol g⁻¹, possibly because of the incorporation of La species into CeO₂ and the formation of La₂O₂CO₃ on CeO₂.

Fig. 5c shows the CO₂-TPD profiles of all the catalysts. The desorption curves of all the samples can be divided into three zones located in the temperature range of 50–200, 200–400, and 400–600 °C, assigned to the weak, medium-strength, and strong basic sites, respectively [4]. It has been reported that medium-strength basic sites play a crucial role in the adsorption and dissociation of CO₂ [45]. The integral area of the

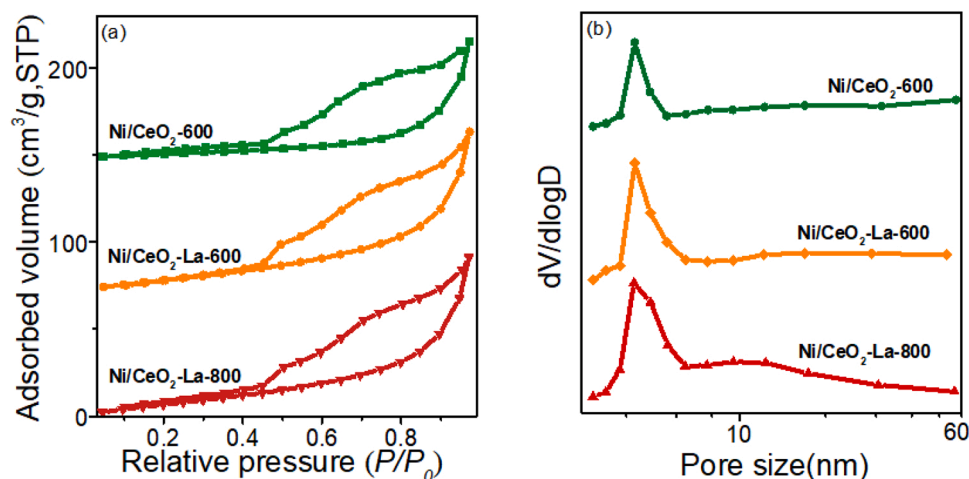


Fig. 4. N₂ adsorption-desorption isotherms (a) and BJH pore size distribution curves (b) of all the catalysts.

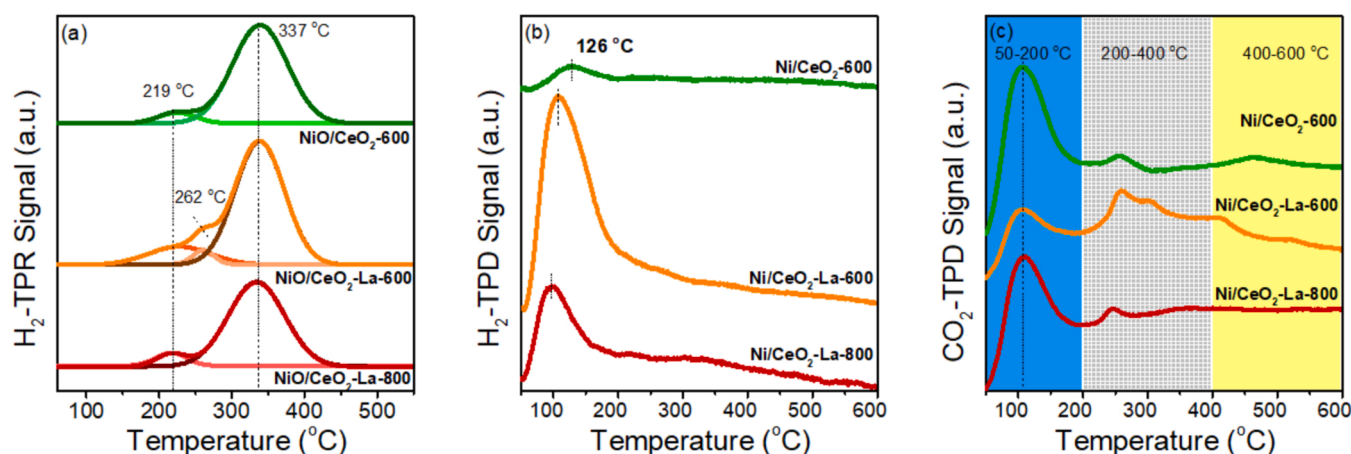


Fig. 5. H₂-TPR profiles (a), H₂-TPD profiles (b), and CO₂-TPD profiles (c) of the various samples.

Table 2

Ni dispersion, H₂ adsorption amount, and TOF of CO₂ value of the samples.

Samples	H ₂ consumption ^a (mmol g ⁻¹)	D ^b (%)	H ₂ uptake ^c (μmol g ⁻¹)	R _w ^d (mol _{CO2} ·g ⁻¹ ·s ⁻¹)	TOF _{CO2} (180 °C) ^e (s ⁻¹)
Ni/ CeO ₂ - 600	7.26	11.32	79.6	9.59 × 10 ⁻⁶	5.0 × 10 ⁻⁴
Ni/ CeO ₂ - La- 600	11.85	28.52	200.5	9.68 × 10 ⁻⁵	1.99 × 10 ⁻³
Ni/ CeO ₂ - La- 800	9.20	15.42	108.4	3.51 × 10 ⁻⁵	1.33 × 10 ⁻³

^a H₂ consumption, calculated based on the H₂-TPR results,

^b Metal dispersion, calculated based on the H₂-TPR and H₂-TPD results,

^c H₂ uptake, calculated based on H₂-TPD results,

^d R_w is the differential rate at 150 °C normalized by the weight of the catalyst,

^e Turnover frequency, calculated based on the metal dispersion and the CO₂ conversion at 180 °C.

zone in the temperature range of 200–400 goes as Ni/CeO₂-600 < Ni/CeO₂-La-800 < Ni/CeO₂-La-600, indicating that Ni/CeO₂-La-600 has the largest number of medium-strength basic sites

because of La doping and the existence of La₂O₂CO₃. Thus, it is anticipated that Ni/CeO₂-La-600 possesses the strongest CO₂ adsorption/-dissociation ability and thus excellent catalytic activity in the CO₂ methanation reaction [47,66].

3.1.6. XPS and Raman analysis

Fig. 6a displays the C 1s spectra of the three catalysts, and each spectrum can be deconvoluted into two peaks at 284.8 and 288.6 eV, assigned to C-C species and carbonates, respectively [53]. The surface CO₃²⁻/(CO₃²⁻ + C) molar ratios can be calculated based on the integrated area of the corresponding peak and are listed in Table 3. The ratio of CO₃²⁻/(CO₃²⁻ + C) on Ni/CeO₂-La-600 (30.7%) is obviously higher than that on both Ni/CeO₂-La-800 (20.9%) and Ni/CeO₂-600 (15.7%), indicating that Ni/CeO₂-La-600 has more surface CO₃²⁻ groups than the others, consistent with the FT-IR result (Fig. 3c). Moreover, Fig. 6b shows the asymmetric O 1s spectra of the three catalysts to provide direct evidence for the effect of doping La³⁺ on the number of oxygen vacancies, in which two peaks are observed: one peak at approximately 529.1 eV (related to lattice oxygen (O_{latt})) and another peak at approximately 531.5 eV (related to surface-adsorbed oxygen species (O_{ads})) [67]. The calculated ratios of O_{ads}/(O_{ads} + O_{latt}) on these catalysts are listed in Table 3, and their ratio values follow Ni/CeO₂-600 (65.9%) < Ni/CeO₂-La-800 (74.3%) < Ni/CeO₂-La-600 (88.2%), suggesting that the introduction of La species into the CeO₂ support can generate more oxygen vacancies and thus more active adsorbed oxygen species. In addition, surface CO₃²⁻ groups on Ni/CeO₂-La-600 also

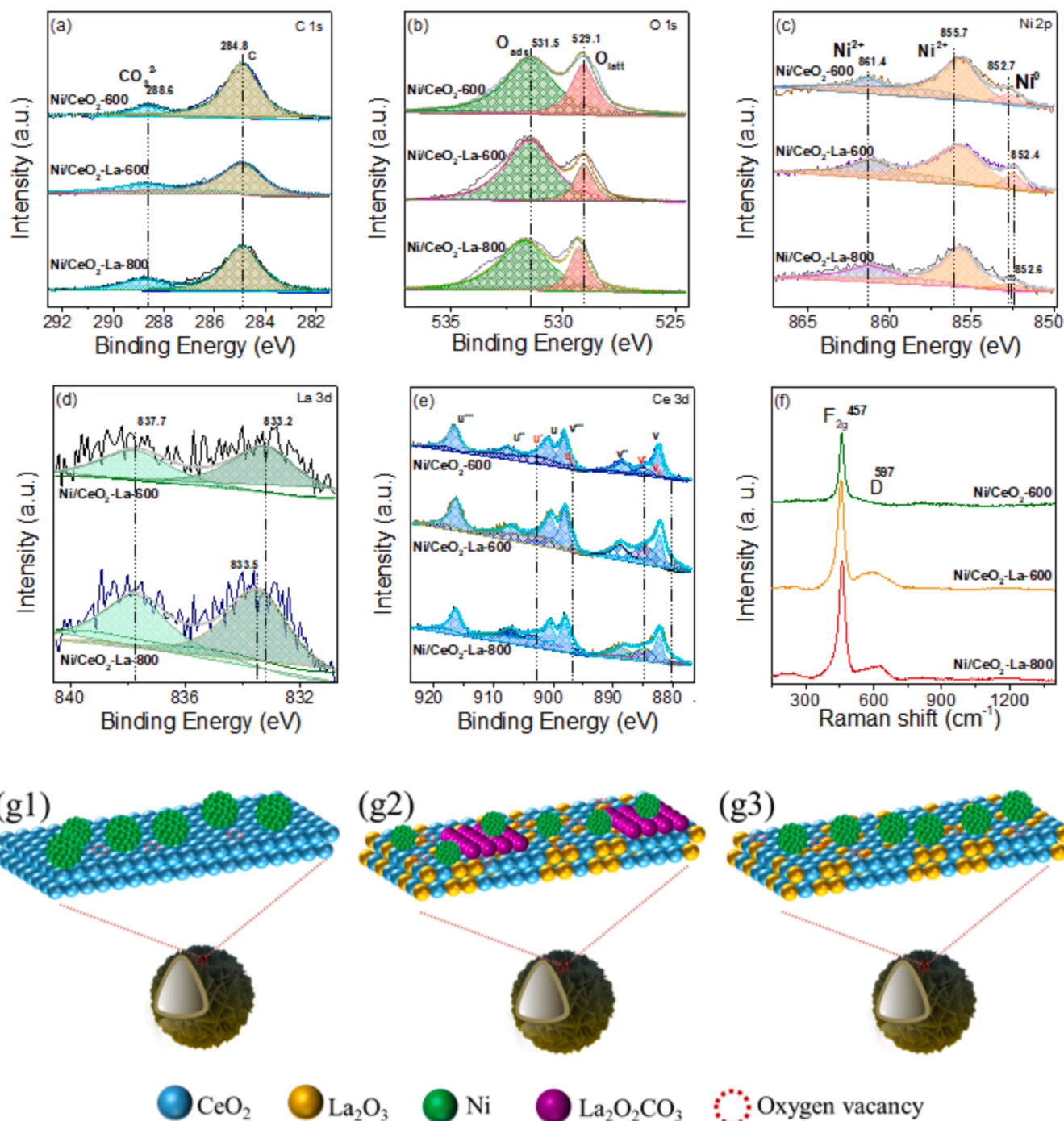


Fig. 6. XPS spectra: O 1 s (a), C 1 s (b), Ni 2p (c), La 3d (d), Ce 3d (e); Raman spectra (f) of the catalysts; and schematic illustration of the structures of Ni/CeO₂-600 (g1), Ni/CeO₂-La-600 (g2), and Ni/CeO₂-La-800 (g3).

provide surface-adsorbed oxygen species.

For the Ni 2p spectra (Fig. 6c), as expected, the Ni⁰ peaks of Ni/CeO₂-600, Ni/CeO₂-La-600, and Ni/CeO₂-La-800 are located at 852.7, 852.4, and 852.6 eV, respectively [68]. These small peak shifts stem from the La³⁺ doping and the increase in the electron cloud density of the Ni atoms (Ni⁰/Ni^{δ-}), which can promote H₂ and CO₂ dissociations on the catalyst surface. In addition, the peaks at 855.7 and 861.4 eV observed on all the catalysts are ascribed to Ni²⁺ [69], possibly due to quick oxidation of metallic Ni in air during sample transfer in the XPS measurement process.

Fig. 6d shows the La 3d XPS spectra of Ni/CeO₂-La-600 and Ni/CeO₂-La-800. Two peaks at 835.4 and 838.8 eV are observed for Ni/CeO₂-La-

600, corresponding to the La³⁺ from La-Ce-O solid solution or La₂O₂CO₃ [60]. However, these peaks for Ni/CeO₂-La-800 shift to lower values of 833.5 and 837.7 eV, respectively, suggesting the presence of some La^{x+} species ($x < 3$) on Ni/CeO₂-La-600. It is known that La^{x+} ($x < 3$) acts as an electron donor that transfers partial electrons to Ni, resulting in an increase in the d-electron density on the surface Ni atoms, which is a crucial factor to improve the catalytic activity [70].

The Ce 3d spectra in Fig. 6e reveal the coexistence of Ce⁴⁺ and Ce³⁺ cations in the near-surface region of all the catalysts. Each spectrum can be deconvoluted into ten peaks. The four peaks denoted as u['], u₀, v['], and v₀ are assigned to surface Ce³⁺, and the other six peaks denoted as u^{'''}, u^{''}, u, v^{'''}, v^{''}, and v are assigned to surface Ce⁴⁺ [71]. The ratio of

Table 3

Catalyst surface quantitative analysis according to the results of XPS and Raman spectra.

Samples	CO ₃ ²⁻ / (CO ₃ ²⁻ + C) molar ratio (%)	O _{ads} /(O _{ads} + O _{lat}) molar ratio (%)	Ce ³⁺ /(Ce ³⁺ + Ce ⁴⁺) molar ratio (%)	La/(La + Ce) Atomic (%)	I _D / I _{F2g}
Ni/CeO ₂ -600	15.7	65.9	17.0	0	0.18
Ni/CeO ₂ -La-600	30.7	88.2	32.2	43.5	0.94
Ni/CeO ₂ -La-800	20.9	74.3	30.0	40.6	0.67

Ce³⁺/(Ce³⁺ + Ce⁴⁺) for these samples, calculated with the integral area of the corresponding signal peak, follows the order of Ni/CeO₂-600 (17.0%) < Ni/CeO₂-La-800 (30.0%) < Ni/CeO₂-La-600 (32.2%) (Table 3), suggesting that La³⁺ doping results in the formation of more surfaces Ce³⁺. Moreover, the surface atomic ratio of La/(La + Ce) on Ni/CeO₂-La-600 is higher than that on Ni/CeO₂-La-800 (Table 3), implying that part of the La³⁺ cations is doped into the CeO₂-La-600 solid solution, and the rest is enriched on its surface in the form of La₂O₂CO₃.

Fig. 6f shows the Raman spectra of all the catalysts, in which there are two peaks at 457 and 595 cm⁻¹, attributed to the F_{2g} octahedrally symmetrical vibration modes and the D stretching vibration caused by the oxygen vacancy, respectively. The peak intensity ratio of the D and F_{2g} modes (I_D/I_{F2g}) reflects the difference in oxygen vacancy concentrations. The ratios of I_D/I_{F2g} in Ni/CeO₂-600, Ni/CeO₂-La-600 and Ni/CeO₂-La-800 are calculated to be 0.18, 0.94, and 0.67, respectively

(Table 3), indicating that doping La³⁺ into CeO₂ can remarkably increase the number of the surface oxygen vacancies because the replacement of two lattice Ce⁴⁺ cations by two La³⁺ cations can lead to the removal of one O ion for maintaining the charge balance. Ni/CeO₂-La-600 has the largest ratio of I_D/I_{F2g} because of the presence of La₂O₂CO₃ on the La-Ce-O solid solution surface.

Based on the above analysis, we can illustrate the structures of Ni/CeO₂-600 (Fig. 6g1), Ni/CeO₂-La-600 (Fig. 6g2), and Ni/CeO₂-La-800 (Fig. 6g3). Ni nanoparticles with a size of ~8.4 nm are supported on the flower-like hollow pure CeO₂-600 microspheres with a low concentration of oxygen vacancies to form the Ni/CeO₂-600 catalyst (Fig. 6g1). For the Ni/CeO₂-La-600 catalyst (Fig. 6g2), smaller Ni nanoparticles (~6.4 nm) are supported on the flower-like hollow La-Ce-O solid solution microspheres, in which part of the La³⁺ cations are permeated into the CeO₂ lattice, leading to more surface oxygen vacancies, and part is enriched on its surface in the form of La₂O₂CO₃. In contrast, in Ni/CeO₂-La-800, La₂O₂CO₃ species are decomposed, and all La³⁺ cations are doped into flower-like hollow CeO₂-La-800 solid solution microspheres (Fig. 6g3). The absence of La₂O₂CO₃ as a physical barrier leads to sintering of the Ni species during the reduction process and forming larger Ni nanoparticles (~7.5 nm).

3.2. Catalytic performance of catalysts

Fig. 7a and b show the CO₂ conversion and CH₄ selectivity of the three catalysts at the WHSV of 30,000 mL g⁻¹ h⁻¹ under 0.1 MPa. For the three catalysts, their CO₂ conversions are in the order of Ni/CeO₂-La-600 > Ni/CeO₂-La-800 > Ni/CeO₂-600 (250–325 °C) (Fig. 7a). The thermodynamic

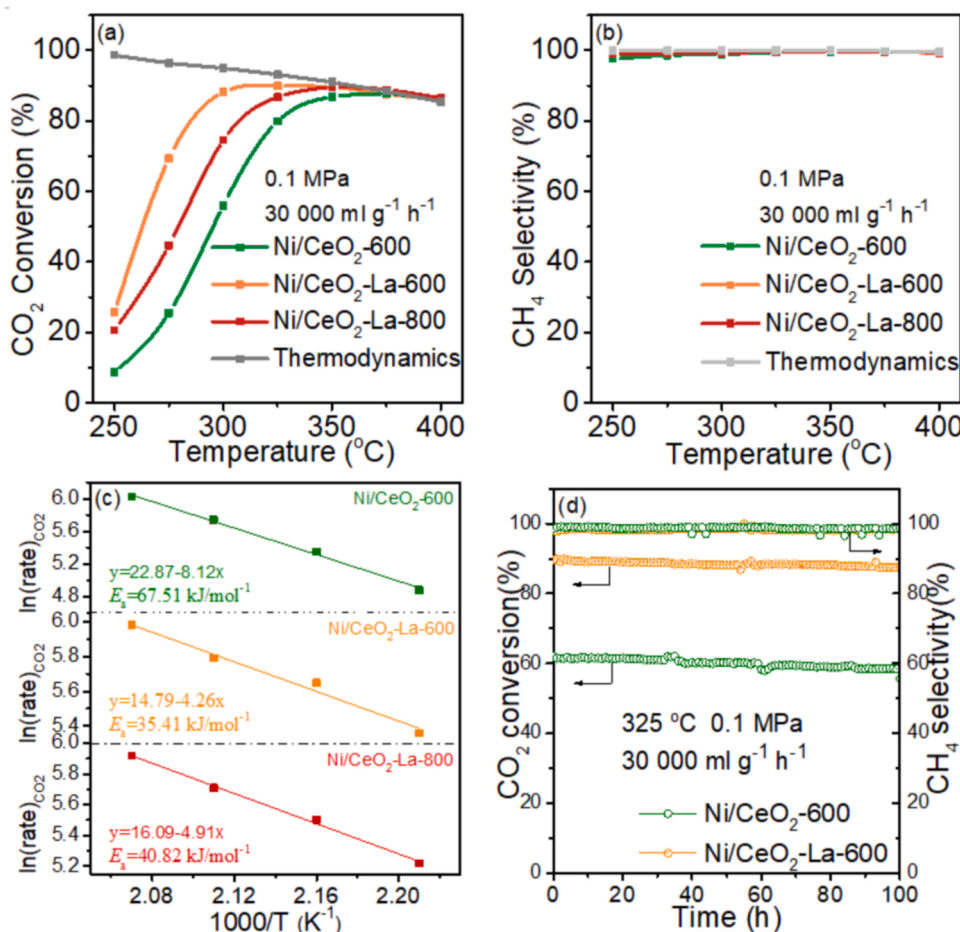


Fig. 7. Catalytic performance of the catalysts: (a) CO₂ conversion; (b) CH₄ selectivity; (c) Arrhenius plot; (d) lifetime test of Ni/CeO₂-600 and Ni/CeO₂-La-600.

equilibrium data are obtained from our previous work [72]. With increasing temperature, the CO₂ conversion of Ni/CeO₂-La-600 reaches the thermodynamic equilibrium at 350 °C, and it still shows the highest activity compared to the other two catalysts. In addition, the CH₄ selectivity over all the catalysts is almost 100% (Fig. 7b), and the main byproduct detected by the gas chromatography is CO, which is derived from the water–gas shift reaction. The CO selectivity was also calculated and shown in Fig. S4. Apparently, the CO selectivity of all the catalysts is below 5% in the range of 250–400 °C. Furthermore, Ni/CeO₂-La-600 shows a higher CO₂ conversion than the Ni-based catalysts reported in the literature (Table 4) [73–75], even a much higher space velocity in this work was used. The Arrhenius plots were obtained at CO₂ conversion less than 10% to exclude the mass and heat transfer effect (Fig. 7c, S3, and S5). The results show that the activation energy has the order of Ni/CeO₂-600 (67.51 kJ mol^{−1}) > Ni/CeO₂-La-800 (40.82 kJ mol^{−1}) > Ni/CeO₂-La-600 (35.41 kJ mol^{−1}), which is highly consistent with the trend of CO₂ methanation activity at atmospheric pressure. According to the Arrhenius equation, the conversion rate of CO₂ (R_w) on Ni/CeO₂-600, Ni/CeO₂-La-600, and Ni/CeO₂-La-800 at 180 °C are calculated to be 9.59×10^{-6} , 9.68×10^{-5} , and 3.51×10^{-5} mol_{CO₂}g^{−1}.s^{−1}, respectively. Ni/CeO₂-La-600 shows the highest R_w, particularly at low temperatures. In addition, based on the results of CO₂ conversion and H₂ adsorption at 180 °C, the TOF values are calculated and listed in Table 2. The TOF_{CO₂} value of Ni/CeO₂-La-600 (1.99×10^{-3} s^{−1}) is much higher than that of Ni/CeO₂-La-800 (1.33×10^{-3} s^{−1}) and even 3.9 times of that of Ni/CeO₂-600 (5.0×10^{-4} s^{−1}). The E_a and TOF values of some other oxide-supported Ni catalysts were also compared in Table S2. The stability tests of Ni/CeO₂-La-600 and Ni/CeO₂-600 were carried out at 325 °C at a WHSV of 30,000 mL g^{−1} h^{−1} for 100 h (Fig. 7d). The CO₂ conversion of Ni/CeO₂-La-600 (~90%) is higher than that of Ni/CeO₂-600 (~61%), and there is no obvious deactivation occurred to the catalyst with ~99% CH₄ selectivity during the 100 h test, indicating the high stability of the catalyst. The Ni crystal sizes of the spent Ni/CeO₂-600 and Ni/CeO₂-La-600 catalysts after the 100 h test are calculated by the XRD patterns (Fig. S6a) to be 14.6 and 10.5 nm, respectively, while those of the fresh catalysts were 12.4 and 6.4 nm, respectively. Therefore, Ni/CeO₂-La-600 shows high anti-sintering performance. For the spent Ni/CeO₂-600, more agglomerated particles can be observed on the CeO₂ surface (Fig. S6b), while the spent Ni/CeO₂-La-600 retains the spherical morphology (Fig. S6c). The above results demonstrate that the La-Ce-O solid solution modified with La₂O₂CO₃ plays an important role in enhancing the catalytic activity and reaction stability of the Ni/CeO₂ catalyst for CO₂ methanation.

3.3. Catalytic mechanism

3.3.1. In situ DRIFTS analysis

Fig. 8a and b show the in situ FTIR spectra of Ni/CeO₂-600 and Ni/CeO₂-La-600 measured in a continuous flow of the reaction gas (V_{H₂}/V_{CO₂} = 4) at different reaction temperatures. For clarity, the band assignments are summarized in Table 5. At low reaction temperatures (50–150 °C), the bands of monodentate carbonate (1516 cm^{−1}), bicarbonate (1461 cm^{−1}) and polydentate carbonate (1425 cm^{−1}) [46] are observed in the spectra of Ni/CeO₂-600 (Fig. 8a). At temperatures above 250 °C, two new bands appear at 1742 and 3016 cm^{−1}, assigned to

CHO* at Ni sites [79] and CH₄ [80], respectively, and their intensity gradually increases with increasing temperature. In contrast, the band of HCOO* at 1365 cm^{−1} does not change significantly with increasing temperature. Moreover, the bands of gas-phase CO (2176 and 2108 cm^{−1}) emerge above 350 °C, derived from the decomposition of the weakly binding HCOO* on Ce³⁺ sites, and they do not participate in further hydrogenation reaction [81]. This observation is consistent with the finding of CO byproducts over Ni/CeO₂-600 in Fig. 7. For Ni/CeO₂-La-600, the variation trends of these bands (Fig. 8b) are different from those of Ni/CeO₂-600. At temperatures below 150 °C, HCOO* (1567 and 1365 cm^{−1}) bands are observed, and their peak intensity increases as the temperature increases, reaches a maximum at 250 °C, then decreases and finally disappears at 400 °C. Moreover, the band of CHO* appears above 150 °C, and its intensity is much stronger than that of Ni/CeO₂-600. In other words, compared with Ni/CeO₂-600, Ni/CeO₂-La-600 has a better ability to adsorb and hydrogenate CO₂ to HCOO*, and to decompose HCOO* to CHO*, which is effective for CO₂ methanation.

Fig. 8c and d show a series of spectra of the two catalysts measured at 300 °C within the inlet gas switched from the initial 4% H₂/1% CO₂/Ar to 10% H₂/Ar. For Ni/CeO₂-600 (Fig. 8c), the bands of HCOO* (1579 and 1302 cm^{−1}), monodentate carbonate (1502 cm^{−1}), and polydentate carbonate (1404 cm^{−1}) are observed in the inlet gas of 4% H₂/1% CO₂/Ar, accompanying with the appearance of the band at 3016 cm^{−1} assigned to CH₄. After switching the inlet gas to 10% H₂/Ar, the HCOO* bands become weak and finally disappear after approximately 15 min, coinciding with the disappearance of the CH₄ peak, indicating that CH₄* is produced by the hydrogenation of HCOO*. In contrast, the bands of the monodentate carbonate and polydentate carbonate are still present with no significant change in their band intensities, further confirming the role of monodentate carbonate and polydentate carbonate as spectators [53]. For the spectra of Ni/CeO₂-La-600 measured in the flow of 4% H₂/1% CO₂/Ar (Fig. 8d), a new band appears at 1740 cm^{−1} attributed to *CHO derived from HCOO* [82]; moreover, the band intensity of HCOO* on it is weaker than that on Ni/CeO₂-600 at the same reaction time. The band intensities of the monodentate carbonate, polydentate carbonate and HCOO* increase with time, although CH₄* was produced initially. This indicates that the rate of CO₂ hydrogenation to HCOO* is greater than HCOO* decomposition followed by hydrogenation to CH₄, thus demonstrating that the decomposition of HCOO* may be a rate-determining step. After switching the gas to 10% H₂/Ar, the HCOO* band became weak rapidly until its complete disappearance after 10 min, much earlier than the case on Ni/CeO₂-600. These results indicate that Ni/CeO₂-La-600 can better decompose HCOO* than Ni/CeO₂-600, which is further confirmed by density functional theory (DFT) calculations (Fig. 9e and f). Duan and coauthors also reported that HCOO* dissociation catalyzed by oxygen vacancies is the rate-determining step in CO₂ methanation.

Fig. 8e shows the in situ FTIR spectra of Ni/CeO₂-600 measured alternately in 1% CO₂/He and 10% H₂/He gases at different times. In the first 0.5 h, 1% CO₂/He is present. Three bands at 1567, 1507, and 1396 cm^{−1} appear, assigned to HCOO*, monodentate and polydentate carbonates, respectively; moreover, these band intensities are almost unchanged with the extension of the adsorption time. Subsequently, the

Table 4
Comparison of activity with the reported catalysts.

Catalyst	Preparation method	H ₂ /CO ₂	CO ₂ Conversion (%)	WHSV (L g ^{−1} h ^{−1})	Temperature (°C)	Pressure (MPa)	Ref.
10Ni/CeO ₂ -La-600	Hydrothermal/impregnation	4:1	88.6	30.0	300	0.1	This work
10Ni/CeO ₂ -La-600	Hydrothermal/impregnation	4:1	90.4	30.0	325	0.1	This work
10%Ni/ZSM-5	Impregnation	4:1	75.0	2.4	400	0.1	[73]
10%Ni-Ce/Al ₂ O ₃	Evaporation induced Self-assembly method	4:1	69.0	15.0	400	0.1	[74]
10%Ni-1MgO/SiO ₂	Co-impregnation method	4:1	67.0	15.0	350	0.1	[76]
10%Ni/CeO ₂	Impregnation	4:1	73.1	22.0	300	0.1	[75]
10%Ni/CeO ₂	Wash-coating	4:1	80.0	14.0	350	0.1	[77]
15%Ni/SBA-15	Hydrothermal	4:1	72.0	10.0	400	0.1	[78]

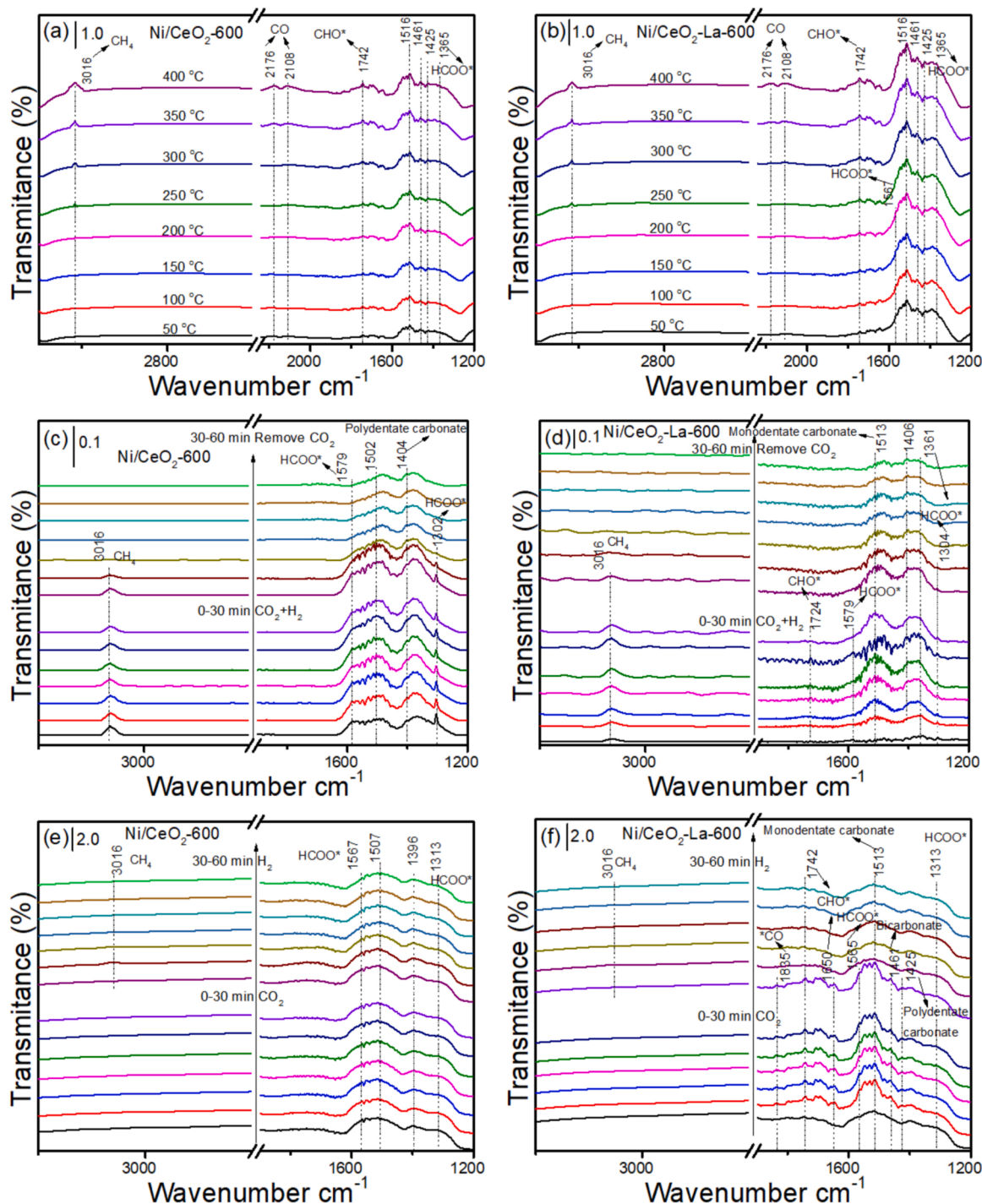


Fig. 8. In situ DRIFTS analysis results on different catalysts in different gases: (a) Ni/CeO₂-600 and (b) Ni/CeO₂-La-600 measured at different reaction temperatures within the inlet gas 4% H₂/1% CO₂/Ar, (c) Ni/CeO₂-600 and (d) Ni/CeO₂-La-600 measured at 300 °C within the inlet gas switched from the initial 4% H₂/1% CO₂/Ar (0–30 min) to 10% H₂/Ar (30–60 min), and (e) Ni/CeO₂-600 and (f) Ni/CeO₂-La-600 within the inlet gas switched from the initial 1% CO₂/He (0–30 min) and 10% H₂/He (30–60 min).

Table 5

The assignments of IR bands [79,83,84].

Wavenumber (cm ⁻¹)	Species	Wavenumber (cm ⁻¹)	Species	Wavenumber (cm ⁻¹)	Species
3750–3598	OH	1838	Bridge- [*] CO	1516	Monodentate carbonate
3016	CH ₄	1742	Formyl, CHO [*]	1461	Bicarbonate
2176, 2108	Gas phase CO	1567, 1365	HCOO [*]	1425	Polydentate carbonate

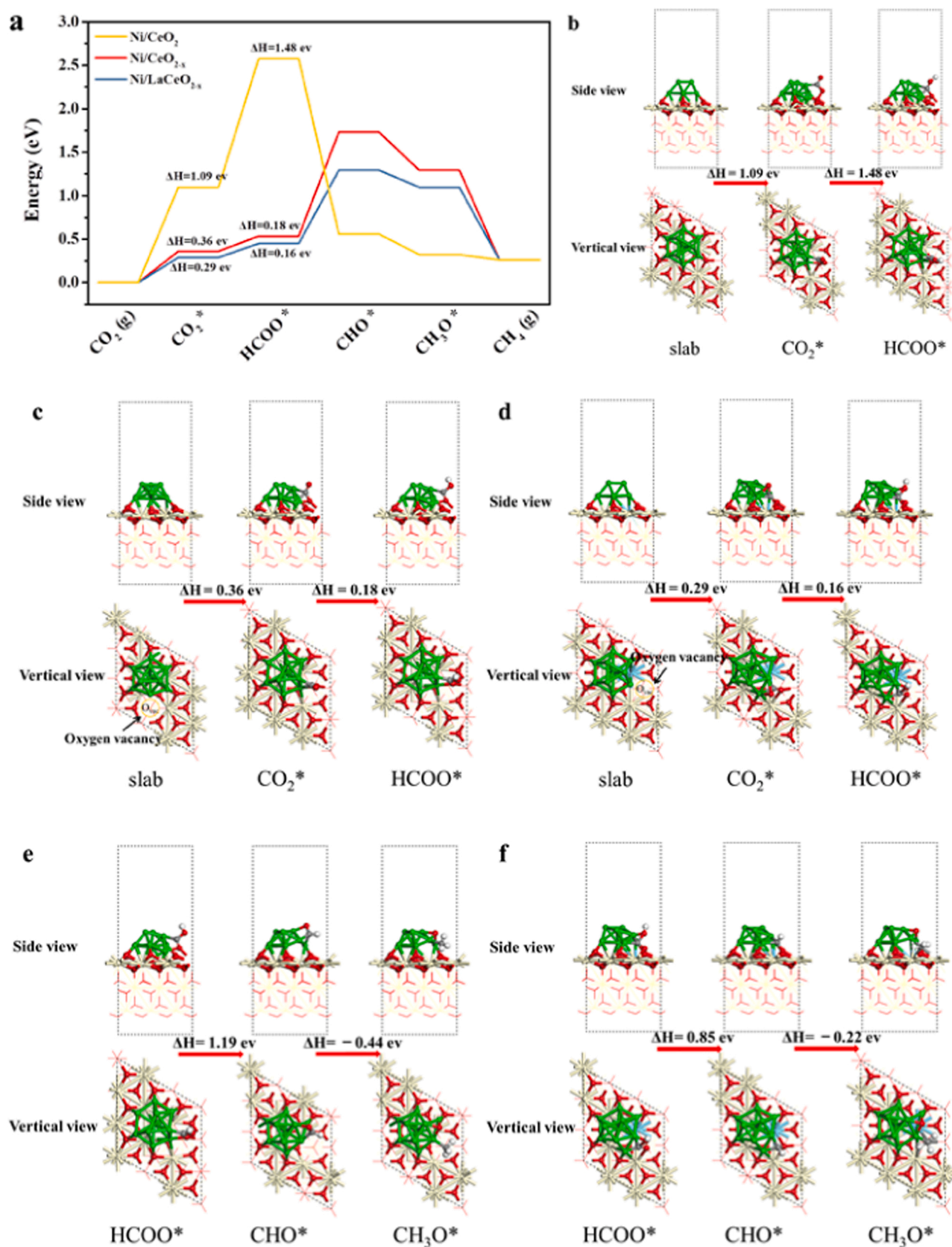


Fig. 9. The energy profiles of the CO₂ reduction on the Ni/CeO₂, Ni/CeO_{2-x}, and Ni/CeO_{2-x}-La catalysts (a); Vertical and side views of intermediate geometries of HCOO* formed on (b) Ni/CeO₂, (c) Ni/CeO_{2-x}, and (d) Ni/CeO_{2-x}-La, intermediate geometries of CH₃O* on (e) Ni/CeO_{2-x} and (f) Ni/CeO_{2-x}-La.

gas was changed to 10% H₂/He during the reaction period of 30 – 60 min. As observed, all of the band intensities do not change significantly, suggesting that Ni/CeO₂-600 has a weak ability to adsorb and activate CO₂. In contrast, once Ni/CeO₂-La-600 is exposed to 1% CO₂/He for 5 min, the bands of adsorbed *CO (1835 cm⁻¹) [53], formyl (1742 and 1650 cm⁻¹) and HCOO* (1565 and 1313 cm⁻¹) species can be observed in the spectra, and their intensities increase with time (Fig. 8f). After switching the gas to 10% H₂/He for 5 min, the intensities of the bands (1565 cm⁻¹) associated with HCOO* are significantly decreased. Simultaneously, the bands of formyl (1742 and 1650 cm⁻¹) and *CO (1835 cm⁻¹) species disappear, whereas a new band at 3016 cm⁻¹ assigned to CH₄ emerges, confirming that the HCOO*, *CHO, and *CO species continue to be hydrogenated to form CH₄. Furthermore, the consumption of *CO is faster than that of HCOO*, suggesting that the surface *CO intermediates are mainly derived from direct CO₂ dissociation rather than the decomposition of HCOO* [19]. These results reveal that the HCOO* pathway existed for CO₂ methanation on the Ni/CeO₂-600 catalyst, while the HCOO* and *CO pathways coexisted on Ni/CeO₂-La-600.

3.3.2. DFT results

To better understand the effect of the oxygen vacancies and La³⁺ doping on CO₂ activation, we carried out the DFT calculations to investigate the reduction of CO₂ to CH₃O* on the surfaces of Ni/CeO₂, Ni/CeO_{2-x} and Ni/CeO_{2-x}-La (Fig. 9a). For Ni/CeO₂ (Fig. 9b) without surface oxygen vacancies, CO₂ molecules tend to be adsorbed at Ni sites to generate adsorbed CO₂* with an adsorption energy of 1.09 eV. These CO₂* species are further hydrogenated to HCOO* by overcoming an energy barrier of 1.48 eV, which acts as the most energy-requiring step. Thus, CO₂* hydrogenation to HCOO* is the rate-determining step on Ni/CeO₂. For Ni/CeO_{2-x} with surface oxygen vacancies (Fig. 9c), the CO₂ adsorption energy is decreased to 0.36 eV, and further hydrogenation to HCOO* is also promoted with an energy barrier of 0.18 eV. Notably, the corresponding energy barriers for the abovementioned two steps are only 0.29 eV and 0.16 eV, respectively, over Ni/CeO_{2-x}-La (Fig. 9d). These results demonstrate that surface oxygen vacancies on the catalysts can promote the conversion of CO₂ to HCOO*. This conclusion is highly in accordance with the in situ FTIR results, which reveal that La³⁺-doped catalysts with more surface oxygen vacancies significantly promote the formation of HCOO* (Fig. 8d). However, the decomposition of HCOO* over Ni/CeO_{2-x} and Ni/CeO_{2-x}-La requires higher activation energy than the other steps, indicating that the rate-determining step on catalysts with oxygen vacancies is HCOO* to CHO, in agreement with the in situ FTIR results (Fig. 8a). In addition,

compared with Ni/CeO_{2-x} (Fig. 9e), HCOO* on Ni/CeO_{2-x}-La dissociates to CHO* (Fig. 9f) more easily, which is conducive to CO₂ methanation.

Herein, the HCOO* route and the *CO route on Ni/CeO_{2-x}-La are evaluated based on the intermediates observed in our in situ DRIFTS experiments and the literature reports [85]. It can be seen that adsorbed CO₂* species can further be hydrogenated to HCOO* by overcoming an energy barrier of 0.16 eV (Fig. 10a). In comparison, the *CO route, in which CO₂* is dissociated to *CO and O*, is energetically favorable (-0.37 eV) (Fig. 10a and b), consistent with the in situ DRIFTS results for *CO intermediates mainly from the direct dissociation of CO₂. The above results serve as additional evidence that the HCOO* and *CO pathways coexisted on Ni/CeO₂-La-600, resulting in a much-increased CO₂ methanation reaction rate.

To understand the crucial role of the surface oxygen vacancy in the formation of CO*, we calculated the energy changes in CO* formation in the absence and presence of surface oxygen vacancy on the catalysts (Fig. 11). In the absence of surface oxygen vacancy, CO₂* is dissociated to CO* with a reaction energy of -0.81 eV (Fig. 11a). In the presence of surface oxygen vacancy, CO₂* is easier to be further dissociated to the adsorbed CO* with a reaction energy of -1.65 eV (Fig. 11b). The results show that the activation of catalysts with the presence of surface oxygen vacancies from CO₂* to CO* is kinetically more favorable than that of catalysts without oxygen vacancies, resulting in the lowest apparent activation energy of Ni/CeO₂-La-600 (Fig. 7c).

3.3.3. Proposed catalytic mechanism on Ni/CeO₂-La-600

Based on our experiment results, we propose the following reaction pathway for the CO₂ methanation on Ni/CeO₂-La-600 (Scheme 1). First, the CO₂ molecules in the gas phase are adsorbed onto the Ni/CeO₂-La-600 surface and react with the active O* (oxygen vacancy) at the Ni-CeO₂-La interface to form OCO₂*. Then, the formed OCO₂* can further react with the dissociated H* to generate hydrogenated carbonates, which can be further hydrogenated to yield HCOO*. On the one hand, this HCOO* intermediate is mainly decomposed to *OCH, which can be converted to methane via *OCH₃ as intermediate species. On the other hand, a small amount of HCOO* dissociates to *CO (Fig. 8b) and is further hydrogenated to CH_x* and the final product of CH₄. Furthermore, the majority of *CO intermediates are derived from the direct dissociation of CO₂, which is kinetically favorable (Figs. 8f and 9a) [19], resulting in a much-increased CO₂ methanation reaction rate [19]. Since the direct dissociation of CO₂ to *CO does not involve multiple thermodynamically stable intermediates, this pathway is more advantageous than that via HCOO* decomposition in kinetics [46,86]. In addition, a small amount of *CO desorbs from the Ce³⁺ sites, and will not

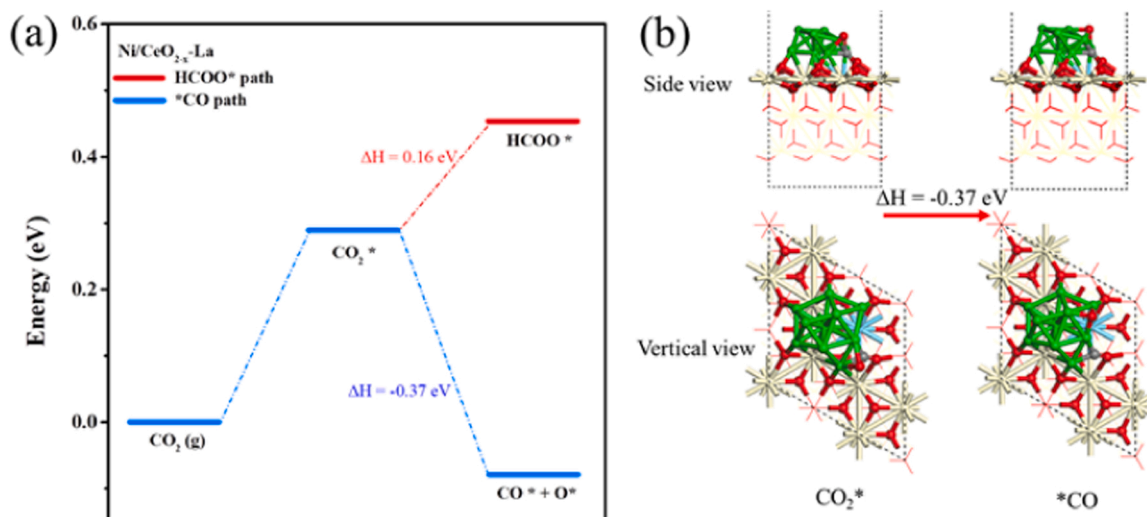


Fig. 10. Energy diagrams for the formation of *CO and HCOO* via the direct CO₂ dissociation and hydrogenation pathways, respectively, on Ni/CeO_{2-x}-La.

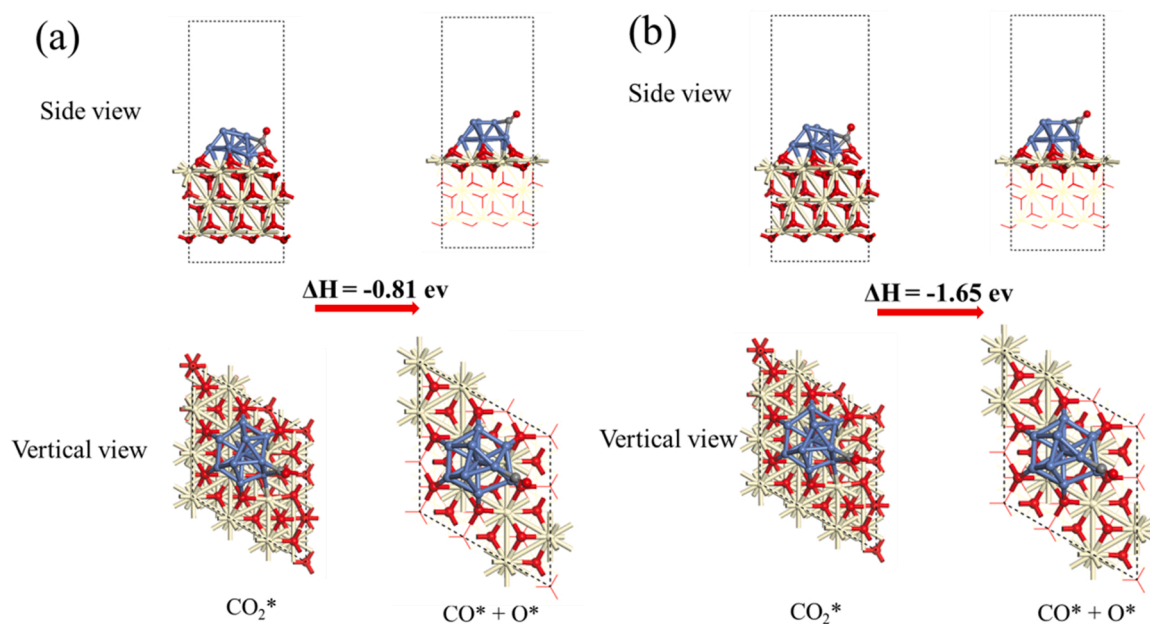
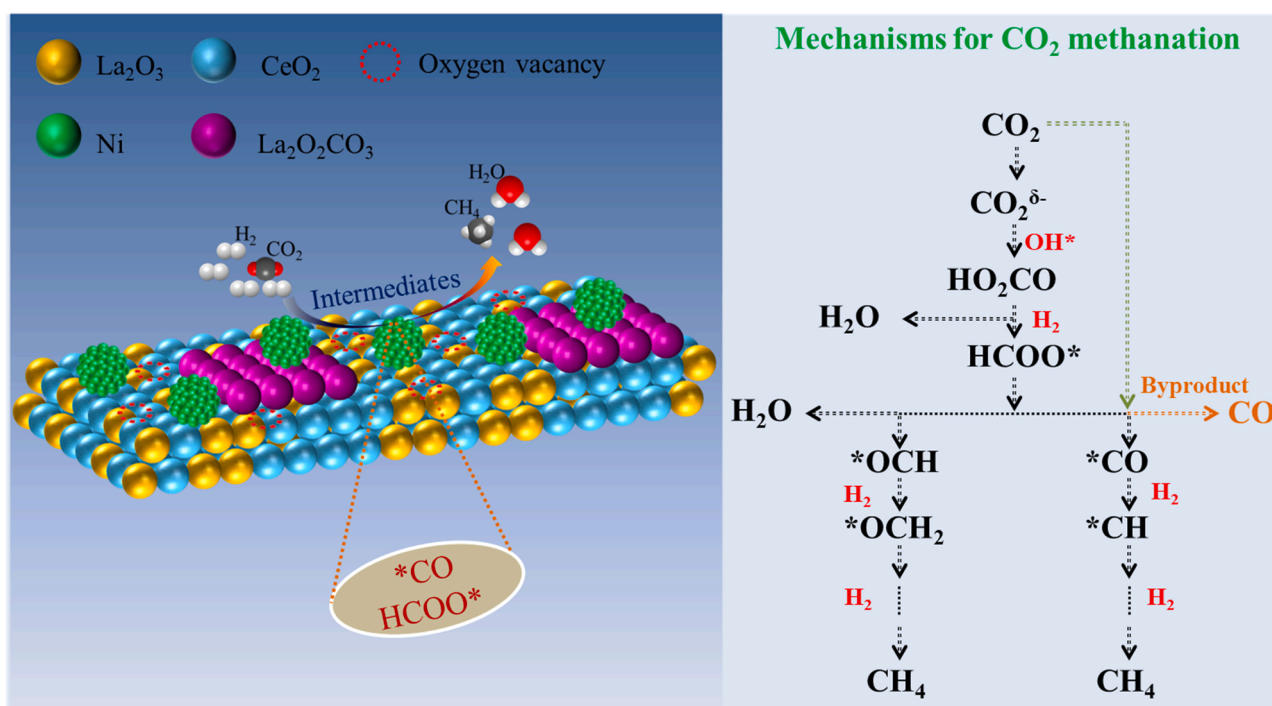


Fig. 11. Formation pathways of CO* on the Ni/CeO₂ (a) and Ni/CeO_{2-x} (b) catalysts.



Scheme 1. The main reaction route of the CO₂ methanation over the Ni/CeO₂-La-600 catalyst.

participate in further hydrogenation reactions [79]. Our in situ FTIR results (Fig. 8) reveal that both the HCOO* and CO routes coexist in CO₂ methanation on the Ni/CeO₂-La-600 surface, consistent with the reported work [82]. However, the pathway of CO₂ to CH₄ over Ni/CeO₂-600 is only via the HCOO* route, in which the gaseous CO₂ molecules react with the surface O₂⁻ species to form HCOO*; then, HCOO* undergoes a series of reactions to form CH₄ (Fig. 8c and e).

4. Conclusions

A new strategy to boost the low-temperature activity of Ni-based catalysts for CO₂ methanation is reported, which is realized by changing the reaction pathway and tuning the rate-determining step, mainly through increasing the surface oxygen vacancy concentration and medium-strength surface basic sites on the catalyst support. For Ni/CeO₂-La-600, La³⁺ cations are doped in the lattice of the CeO₂ to form a solid solution structure accompanied by the formation of a layer of the La₂O₂CO₃ modifier. This structure has much more surface oxygen

vacancies and medium-strength surface basic sites than Ni/CeO₂-La-800 and Ni/CeO₂-600. In situ FTIR and DFT calculation results show that CO₂ methanation on Ni/CeO₂-La-600 follows both the HCOO* and the *CO pathways, while on Ni/CeO₂-600, it occurs only via the HCOO* pathway. Moreover, most *CO intermediates on Ni/CeO₂-La-600 are derived from the direct dissociation of CO₂, which is kinetically more favorable, resulting in its much-increased CO₂ methanation activity at low temperatures. DFT calculations also show that the rate-determining step on Ni/CeO₂-600 with fewer oxygen vacancies is CO₂ * hydrogenated to HCOO*, while that on Ni/CeO₂-La-600 is through HCOO* to CHO with a lower energy barrier than the former. It is believed that the HCOO* pathway over Ni/CeO₂-La-600 is more favorable kinetically than that over Ni/CeO₂-600. The work provides new insights into the CO₂ hydrogenation on the Ni-based catalysts.

CRediT authorship contribution statement

Tengfei Zhang: Methodology, Validation, Formal analysis, Investigation, Data curation, Writing – original draft, Visualization. **Weiwei Wang:** Methodology, Software, Data curation. **Fangna Gu:** Conceptualization, Methodology, Writing – review & editing, Visualization, Supervision, Project administration, Funding acquisition. **Wenqing Xu:** Methodology, Writing – review & editing, Visualization. **Jianling Zhang:** Resources. **Zhenxing Li:** Writing – review & editing. **Tingyu Zhu:** Writing – review & editing. **Guangwen Xu:** Writing – review & editing. **Ziyi Zhong:** Writing – review & editing. **Fabing Su:** Writing – review & editing, Visualization, Supervision, Project administration, Funding acquisition.

Declaration of Competing Interest

The authors declare that they have no known competing financial interests or personal relationships that could have appeared to influence the work reported in this paper.

Acknowledgement

This research was funded by the National Natural Science Foundation of China (21776286) and National Key Research and Development Program of China (No. 2018YFB0604501). Ziyi Zhong thanks the financial support from 2020 Li Ka Shing Foundation Cross-Disciplinary Research Grant (2020LKSFG09A) and Guangdong Province Key Discipline Fund (GTIIT).

Appendix A. Supporting information

Supplementary data associated with this article can be found in the online version at [doi:10.1016/j.apcatb.2022.121385](https://doi.org/10.1016/j.apcatb.2022.121385).

References

- G. Wang, R. Luo, C. Yang, J. Song, C. Xiong, H. Tian, Z. Zhao, R. Mu, J. Gong, Active sites in CO₂ hydrogenation over confined VO_x-Rh catalysts, *Sci. China Chem.* 62 (2019) 1710–1719.
- S. Rönisch, J. Schneider, S. Matthischke, M. Schlüter, M. Götz, J. Lefebvre, P. Prabhakaran, S. Bajohr, Review on methanation—from fundamentals to current projects, *Fuel* 166 (2016) 276–296.
- I. Sreedhar, Y. Varun, S.A. Singh, A. Venugopal, B.M. Reddy, Developmental trends in CO₂ methanation using various catalysts, *Catal. Sci. Technol.* 9 (2019) 4478–4504.
- F. He, J. Zhuang, B. Lu, X. Liu, J. Zhang, F. Gu, M. Zhu, J. Xu, Z. Zhong, G. Xu, F. Su, Ni-based catalysts derived from Ni-Zr-Al ternary hydrotalcites show outstanding catalytic properties for low-temperature CO₂ methanation, *Appl. Catal., B* 293 (2021), 120218.
- S. Abate, C. Mebrahtu, E. Giglio, F. Deorsola, S. Bensaid, S. Perathoner, R. Pirone, G. Centi, Catalytic performance of γ -Al₂O₃-ZrO₂-TiO₂-CeO₂ composite oxide supported Ni-based catalysts for CO₂ methanation, *Ind. Eng. Chem. Res.* 55 (2016) 4451–4460.
- T.A. Le, M.S. Kim, S.H. Lee, T.W. Kim, E.D. Park, CO and CO₂ methanation over supported Ni catalysts, *Catal. Today* 293–294 (2017) 89–96.
- K. Zhao, W. Wang, Z. Li, Highly efficient Ni/ZrO₂ catalysts prepared via combustion method for CO₂ methanation, *J. CO₂ Util.* 16 (2016) 236–244.
- T. Zhang, Q. Liu, Lanthanum-modified MCF-derived nickel phyllosilicate catalyst for enhanced CO₂ methanation: a comprehensive study, *ACS Appl. Mater. Interfaces* 12 (2020) 19587–19600.
- T. Zhang, H. Ai, Q. Liu, La₂O₃-promoted Ni/Al₂O₃ catalyst for CO methanation: enhanced catalytic activity and stability, *Energy Technol.* 7 (2019), 1900531.
- Q. Liu, F. Gu, J. Gao, H. Li, G. Xu, F. Su, Coking-resistant Ni-ZrO₂/Al₂O₃ catalyst for CO methanation, *J. Energy Chem.* 23 (2014) 761–770.
- W. Xing, Y. Liu, W. Zhang, Y. Sun, X. Kai, T. Yang, Study on methanation performance of biomass gasification syngas based on a Ni/Al₂O₃ monolithic catalyst, *ACS Omega* 5 (2020) 28597–28605.
- K. Wang, Y. Men, S. Liu, J. Wang, Y. Li, Y. Tang, Z. Li, W. An, X. Pan, L. Li, Decoupling the size and support/metal loadings effect of Ni/SiO₂ catalysts for CO₂ methanation, *Fuel* 304 (2021), 121388.
- R. Zhou, N. Rui, Z. Fan, C.-J. Liu, Effect of the structure of Ni/TiO₂ catalyst on CO₂ methanation, *Int. J. Hydrog. Energ.* 41 (2016) 22017–22025.
- L. Wang, J. Hu, H. Liu, Q. Wei, D. Gong, L. Mo, H. Tao, C. Zhang, Three-dimensional mesoporous Ni-CeO₂ catalysts with Ni embedded in the pore walls for CO₂ methanation, *Catalysts* 10 (2020) 523.
- Y. Yan, Y. Dai, H. He, Y. Yu, Y. Yang, A novel W-doped Ni-Mg mixed oxide catalyst for CO₂ methanation, *Appl. Catal., B* 196 (2016) 108–116.
- J. Gödde, M. Merko, W. Xia, M. Muhler, Nickel nanoparticles supported on nitrogen-doped carbon nanotubes are a highly active, selective and stable CO₂ methanation catalyst, *J. Energy Chem.* 54 (2021) 323–331.
- M.C. Bacariza, I. Graça, J.M. Lopes, C. Henriques, Enhanced activity of CO₂ hydrogenation to CH₄ over Ni based zeolites through the optimization of the Si/Al ratio, *Microporous Mesoporous Mater.* 267 (2018) 9–19.
- D.C.D. da Silva, S. Letichevsky, L.E.P. Borges, L.G. Appel, The Ni/ZrO₂ catalyst and the methanation of CO and CO₂, *Int. J. Hydrog. Energ.* 37 (2012) 8923–8928.
- M. Zhu, P. Tian, X. Cao, J. Chen, T. Pu, B. Shi, J. Xu, J. Moon, Z. Wu, Y. Han, Vacancy engineering of the nickel-based catalysts for enhanced CO₂ methanation, *Appl. Catal., B* 282 (2021), 119561.
- M. Li, H. Amari, A.C. van Veen, Metal-oxide interaction enhanced CO₂ activation in methanation over ceria supported nickel nanocrystallites, *Appl. Catal., B* 239 (2018) 27–35.
- R. Tang, N. Ullah, Y. Hui, X. Li, Z. Li, Enhanced CO₂ methanation activity over Ni/CeO₂ catalyst by one-pot method, *Mol. Catal.* 508 (2021), 111602.
- X. Feng, K. Wang, M. Zhou, F. Li, J. Liu, M. Zhao, L. Zhao, X. Song, P. Zhang, L. Gao, Metal organic framework derived Ni/CeO₂ catalyst with highly dispersed ultra-fine Ni nanoparticles: Impregnation synthesis and the application in CO₂ methanation, *Ceram. Int.* 47 (2021) 12366–12374.
- Y. Du, C. Qin, Y. Xu, D. Xu, J. Bai, G. Ma, M. Ding, Ni nanoparticles dispersed on oxygen vacancies-rich CeO₂ nanoplates for enhanced low-temperature CO₂ methanation performance, *Chem. Eng. J.* 418 (2021), 129402.
- Y. Ma, J. Liu, M. Chu, J. Yue, Y. Cui, G. Xu, Enhanced low-temperature activity of CO₂ methanation over Ni/CeO₂ catalyst, *Catal. Lett.* 152 (2022) 872–882.
- N. Hashimoto, K. Mori, K. Asahara, S. Shibata, H. Jida, Y. Kuwahara, H. Yamashita, How the morphology of NiO_x-decorated CeO₂ nanostructures affects catalytic properties in CO₂ methanation, *Langmuir* 37 (2021) 5376–5384.
- H. Mai, L. Sun, Y. Zhang, R. Si, W. Feng, H. Zhang, H. Liu, C. Yan, Shape-selective synthesis and oxygen storage behavior of ceria nanopolyhedra, nanorods, and nanocubes, *J. Phys. Chem. B* 109 (2005) 24380–24385.
- Y. Zhang, T. Zhang, F. Wang, Q. Zhu, Q. Liu, Ni/CeO₂ catalysts for low-temperature CO₂ methanation: identifying effect of support morphology and oxygen vacancy, *6 (2021) 1222–1233*.
- J. Zhang, H. Kumagai, K. Yamamura, S. Ohara, S. Takami, A. Morikawa, H. Shinjoh, K. Kaneko, T. Adschiri, A. Suda, Extra-low-temperature oxygen storage capacity of CeO₂ nanocrystals with cubic facets, *Nano Lett.* 11 (2011) 361–364.
- S. Ratchahat, S. Surathitmethakul, A. Thamunkit, P. Mala, M. Sudoh, R. Watanabe, C. Fukuhara, S.S. Chen, K.C.W. Wu, T. Charinpanitkul, Catalytic performance of Ni/CeO₂ catalysts prepared from different routes for CO₂ methanation, *J. Taiwan Inst. Chem. Eng.* 121 (2021) 184–196.
- C. Sun, G. Xiao, H. Li, L. Chen, Mesoscale organization of flower-like La₂O₂CO₃ and La₂O₃ microspheres, *90 (2007) 2576–2581*.
- H. Li, G. Lu, Q. Dai, Y. Wang, Y. Guo, Y. Guo, Hierarchical organization and catalytic activity of high-surface-area mesoporous ceria microspheres prepared via hydrothermal routes, *ACS Appl. Mater. Interfaces* 2 (2010) 838–846.
- X. Hu, J. Yang, W. Sun, N. Wang, S. An, Q. Wang, Y. Zhang, X. Xie, L. Huang, Y-Zr-O solid solution supported Ni-based catalysts for hydrogen production via auto-thermal reforming of acetic acid, *Appl. Catal., B* 278 (2020), 119264.
- X. Han, Y. Wang, H. Hao, R. Guo, Y. Hu, W. Jiang, Ce_{1-x}La_xO₃ solid solution prepared from mixed rare earth chloride for soot oxidation, *J. Rare Earths* 34 (2016) 590–596.
- Z. Xiao, C. Wu, L. Wang, J. Xu, Q. Zheng, L. Pan, J. Zou, X. Zhang, G. Li, Boosting hydrogen production from steam reforming of ethanol on nickel by lanthanum doped ceria, *Appl. Catal., B* 286 (2021), 119884.
- Q. Liu, J. Sun, Q. Feng, S. Ji, Z. Wang, A La-promoted Ni/MgAl₂O₄ catalyst with superior methanation performance for the production of synthetic natural gas, *Catal. Today* 339 (2020) 127–134.
- G. Garbarino, C. Wang, T. Cavattoni, E. Finocchio, P. Riani, M. Flytzani-Stephanopoulos, G. Busca, A study of Ni/La-Al₂O₃ catalysts: A competitive system for CO₂ methanation, *Appl. Catal., B* 248 (2019) 286–297.
- H. Chen, Y. Mu, Y. Shao, S. Chansai, S. Xu, C.E. Stere, H. Xiang, R. Zhang, Y. Jiao, C. Hardacre, X. Fan, Coupling non-thermal plasma with Ni catalysts supported on

- BETA zeolite for catalytic CO₂ methanation, *Catal. Sci. Technol.* 9 (2019) 4135–4145.
- [38] L. Dou, M. Fu, Y. Gao, L. Wang, C. Yan, T. Ma, Q. Zhang, X. Li, Efficient sulfur resistance of Fe, La and Ce doped hierarchically structured catalysts for low-temperature methanation integrated with electric internal heating, *Fuel* 283 (2021), 118984.
- [39] X. Wang, L. Zhu, Y. Zhuo, Y. Zhu, S. Wang, Enhancement of CO₂ methanation over La-modified Ni/SBA-15 catalysts prepared by different doping methods, *ACS Sustain. Chem. Eng.* 7 (2019) 14647–14660.
- [40] L. Xu, X. Wen, M. Chen, C. Lv, Y. Cui, X. Wu, C. Wu, Z. Miao, X. Hu, Highly dispersed Ni-La catalysts over mesoporous nanosponge MFI zeolite for low-temperature CO₂ methanation: Synergistic effect between mesoporous and microporous channels, *J. Ind. Eng. Chem.* 100 (2021) 159–173.
- [41] G.I. Siakavelas, N.D. Charisiou, A. AlKhoori, S. AlKhoori, V. Sebastian, S.J. Hinder, M.A. Baker, I.V. Yentekakis, K. Polychronopoulou, M.A. Goula, Highly selective and stable Ni/La-M (M=Sm, Pr, and Mg)-CeO₂ catalysts for CO₂ methanation, *J. CO₂ Util.* 51 (2021), 101618.
- [42] C. Liang, T. Wei, H. Wang, Z. Yu, D. Dong, S. Zhang, Q. Liu, G. Hu, X. Hu, Impacts of La addition on formation of the reaction intermediates over alumina and silica supported nickel catalysts in methanation of CO₂, *J. Energy Inst.* 93 (2020) 723–738.
- [43] J. Li, Q. Song, J. Li, S. Yang, Y. Gao, Q. Wang, F. Yu, La-enhanced Ni nanoparticles highly dispersed on SiC for low-temperature CO methanation performance, *Rare Met.* 40 (2021) 1753–1761.
- [44] P. Riani, I. Valsamakis, T. Cavattoni, V. Sanchez Escribano, G. Busca, G. Garbarino, Ni/SiO₂-Al₂O₃ catalysts for CO₂ methanation: Effect of La₂O₃ addition, *Appl. Catal., B* 284 (2021), 119697.
- [45] Y. Dai, M. Xu, Q. Wang, R. Huang, Y. Jin, B. Bian, C. Tumurbaatar, B. Ishtsog, T. Bold, Y. Yang, Enhanced activity and stability of Ni/La₂O₃CO₃ catalyst for CO₂ methanation by metal-carbonate interaction, *Appl. Catal., B* 277 (2020), 119271.
- [46] X. Jia, X. Zhang, N. Rui, X. Hu, C. Liu, Structural effect of Ni/ZrO₂ catalyst on CO₂ methanation with enhanced activity, *Appl. Catal., B* 244 (2019) 159–169.
- [47] H. Muroyama, Y. Tsuda, T. Asakoshi, H. Masitah, T. Okanishi, T. Matsui, K. Eguchi, Carbon dioxide methanation over Ni catalysts supported on various metal oxides, *J. Catal.* 343 (2016) 178–184.
- [48] Y. Tang, Y. Wei, Z. Wang, S. Zhang, Y. Li, L. Nguyen, Y. Li, Y. Zhou, W. Shen, F. Tao, P. Hu, Synergy of single-atom NiI and RuI sites on CeO₂ for dry reforming of CH₄, *J. Am. Chem. Soc.* 141 (2019) 7283–7293.
- [49] D. Ding, W. Lu, Y. Xiong, X. Pan, J. Zhang, C. Ling, Y. Du, Q. Xue, Facile synthesis of La₂O₃/CO₃ nanoparticle films and its CO₂ sensing properties and mechanisms, *Appl. Surf. Sci.* 426 (2017) 725–733.
- [50] W. Sun, Y. Gao, G. Zhao, J. Si, Y. Liu, Y. Lu, Mn₂O₃-Na₂WO₄ doping of CexZr_{1-x}O₂ enables increased activity and selectivity for low temperature oxidative coupling of methane, *J. Catal.* 400 (2021) 372–386.
- [51] C. Zhou, H. Zhang, Z. Zhang, L. Li, Improved reactivity for toluene oxidation on MnO_x/CeO₂-ZrO₂ catalyst by the synthesis of cubic-tetragonal interfaces, *Appl. Surf. Sci.* 539 (2021), 148188.
- [52] A. Joseph, K.P. John Mathew, S. Vandana, Zirconium-doped ceria nanoparticles as anticorrosion pigments in waterborne epoxy-polymer coatings, *ACS Appl. Nano Mater.* 4 (2021) 834–849.
- [53] X. Xu, L. Liu, Y. Tong, X. Fang, J. Xu, D.-E. Jiang, X. Wang, Facile Cr³⁺-doping strategy dramatically promoting Ru/CeO₂ for low-temperature CO₂ methanation: Unraveling the roles of surface oxygen vacancies and hydroxyl groups, *ACS Catal.* 11 (2021) 5762–5775.
- [54] M. Jobbágy, C. Sorbello, E.E. Sileo, Crystalline Ce(III)–La(III) double basic carbonates: a chemical shortcut to obtain nanometric La(III)-doped ceria, *J. Phys. Chem. C* 113 (2009) 10853–10857.
- [55] Q. Wang, Y. Gao, C. Tumurbaatar, T. Bold, F. Wei, Y. Dai, Y. Yang, Tuned selectivity and enhanced activity of CO₂ methanation over Ru catalysts by modified metal-carbonate interfaces, *J. Energy Chem.* 64 (2022) 38–46.
- [56] M. Myint, Y. Yan, J.G. Chen, Reaction pathways of propanal and 1-propanol on Fe/Ni(111) and Cu/Ni(111) bimetallic surfaces, *J. Phys. Chem. C* 118 (2014) 11340–11349.
- [57] J. Carrasco, L. Barrio, P. Liu, J.A. Rodriguez, M.V. Ganduglia-pirovano, theoretical studies of the adsorption of CO and C on Ni(111) and Ni/CeO₂(111): Evidence of a strong metal-support interaction, *J. Phys. Chem. C* 117 (2013) 8241–8250.
- [58] Y. Yu, G. Jin, Y. Wang, X. Guo, Synthesis of natural gas from CO methanation over SiC supported Ni-Co bimetallic catalysts, *Catal. Commun.* 31 (2013) 5–10.
- [59] K. Michalska, P. Kowalik, W. Próchniak, T. Borowiecki, The effect of La₂O₃ on Ni/Al₂O₃ catalyst for methanation at very low CO_x/H₂ ratio, *Catal. Lett.* 148 (2018) 972–978.
- [60] D. Méndez-Mateos, V.L. Barrio, J.M. Requies, J.F. Cambra, Effect of the addition of alkaline earth and lanthanide metals for the modification of the alumina support in Ni and Ru catalysts in CO₂ methanation, *Catalysts* 11 (2021) 353.
- [61] G. Botzolak, G. Goula, A. Rontogianni, E. Nikolarak, N. Chalmers, P. Zygouri, M. Karakassides, D. Gournis, N. Charisiou, M. Goula, S. Papadopoulos, I. Yentekakis, CO₂ methanation on supported Rh nanoparticles: the combined effect of support oxygen storage capacity and Rh particle size, *Catalysts* 10 (2020) 944.
- [62] E. Nikolarak, G. Goula, P. Panagiotopoulou, M.J. Taylor, K. Kousi, G. Kyriakou, D. I. Kondarides, R.M. Lambert, I.V. Yentekakis, Support induced effects on the ir nanoparticles activity, selectivity and stability performance under CO₂ reforming of methane, *Nanomaterials* 11 (2021) 2880.
- [63] I.V. Yentekakis, G. Goula, M. Hatzisymeon, I. Betsi-Argyropoulou, G. Botzolak, K. Kousi, D.I. Kondarides, M.J. Taylor, C.M.A. Parlett, A. Osatiashtiani, G. Kyriakou, J.P. Holgado, R.M. Lambert, Effect of support oxygen storage capacity on the catalytic performance of Rh nanoparticles for CO₂ reforming of methane, *Appl. Catal., B* 243 (2019) 490–501.
- [64] E. Aneggi, D. Wiater, C. de Leitenburg, J. Llorca, A. Trovarelli, Shape-dependent activity of ceria in soot combustion, *ACS Catal.* 4 (2014) 172–181.
- [65] J. Gao, C. Jia, J. Li, F. Gu, G. Xu, Z. Zhong, F. Su, Nickel catalysts supported on barium hexaaluminate for enhanced CO methanation, *Ind. Eng. Chem. Res.* 51 (2012) 10345–10353.
- [66] X. Li, D. Li, H. Tian, L. Zeng, Z. Zhao, J. Gong, Dry reforming of methane over Ni/La₂O₃ nanorod catalysts with stabilized Ni nanoparticles, *Appl. Catal., B* 202 (2017) 683–694.
- [67] N. Rui, X. Zhang, F. Zhang, Z. Liu, X. Cao, Z. Xie, R. Zou, S.D. Senanayake, Y. Yang, J.A. Rodriguez, C.-J. Liu, Highly active Ni/CeO₂ catalyst for CO₂ methanation: Preparation and characterization, *Appl. Catal., B* 282 (2021), 119581.
- [68] J. Liu, C. Li, F. Wang, S. He, H. Chen, Y. Zhao, M. Wei, D.G. Evans, X. Duan, Enhanced low-temperature activity of CO₂ methanation over highly-dispersed Ni/TiO₂ catalyst, *Catal. Sci. Technol.* 3 (2013) 2627–2633.
- [69] J. Xu, C. Sun, Z. Wang, Y. Hou, Z. Ding, S. Wang, Perovskite oxide LaNiO₃ nanoparticles for boosting H₂ evolution over commercial CdS with visible light, *24* (2018) 18512–18517.
- [70] Q. Liu, H. Yang, H. Dong, W. Zhang, B. Bian, Q. He, J. Yang, X. Meng, Z. Tian, G. Zhao, Effects of preparation method and Sm₂O₃ promoter on CO methanation by a mesoporous NiO-Sm₂O₃/Al₂O₃ catalyst, *N. J. Chem.* 42 (2018) 13096–13106.
- [71] L. Xu, X. Wen, M. Chen, C. Lv, Y. Cui, X. Wu, C. Wu, B. Yang, Z. Miao, X. Hu, Mesoporous Ce-Zr solid solutions supported Ni-based catalysts for low-temperature CO₂ methanation by tuning the reaction intermediates, *Fuel* 282 (2020), 118813.
- [72] J. Gao, Y. Wang, Y. Ping, D. Hu, G. Xu, F. Gu, F. Su, A thermodynamic analysis of methanation reactions of carbon oxides for the production of synthetic natural gas, *RSC Adv.* 2 (2012) 2358–2368.
- [73] X. Guo, A. Traitangwong, M. Hu, C. Zuo, V. Meeyoo, Z. Peng, C. Li, Carbon dioxide methanation over nickel-based catalysts supported on various mesoporous material, *Energy Fuels* 32 (2018) 3681–3689.
- [74] L. Xu, F. Wang, M. Chen, D. Nie, X. Lian, Z. Lu, H. Chen, K. Zhang, P. Ge, CO₂ methanation over rare earth doped Ni based mesoporous catalysts with intensified low-temperature activity, *Int. J. Hydrog. Energ.* 42 (2017) 15523–15539.
- [75] G. Zhou, H. Liu, K. Cui, A. Jia, G. Hu, Z. Jiao, Y. Liu, X. Zhang, Role of surface Ni and Ce species of Ni/CeO₂ catalyst in CO₂ methanation, *Appl. Surf. Sci.* 383 (2016) 248–252.
- [76] M. Guo, G. Lu, The effect of impregnation strategy on structural characters and CO₂ methanation properties over MgO modified Ni/SiO₂ catalysts, *Catal. Commun.* 54 (2014) 55–60.
- [77] C. Fukuhara, K. Hayakawa, Y. Suzuki, W. Kawasaki, R. Watanabe, A novel nickel-based structured catalyst for CO₂ methanation: a honeycomb-type Ni/CeO₂ catalyst to transform greenhouse gas into useful resources, *Appl. Catal., A* 532 (2017) 12–18.
- [78] Q. Liu, Y. Tian, One-pot synthesis of NiO/SBA-15 monolith catalyst with a three-dimensional framework for CO₂ methanation, *Int. J. Hydrog. Energ.* 42 (2017) 12295–12300.
- [79] R. Ye, Q. Li, W. Gong, T. Wang, J.J. Razink, L. Lin, Y. Qin, Z. Zhou, H. Adidharma, J. Tang, A.G. Russell, M. Fan, Y. Yao, High-performance of nanostructured Ni/CeO₂ catalyst on CO₂ methanation, *Appl. Catal., B* 268 (2020), 118474.
- [80] P.R.L. Keating, D.O. Scanlon, G.W. Watson, The nature of oxygen states on the surfaces of CeO₂ and La-doped CeO₂, *Chem. Phys. Lett.* 608 (2014) 239–243.
- [81] Y. Yu, Y. Chan, Z. Bian, F. Song, J. Wang, Q. Zhong, S. Kawi, Enhanced performance and selectivity of CO₂ methanation over g-C₃N₄ assisted synthesis of NiCeO₂ catalyst: Kinetics and DRIFTS studies, *Int. J. Hydrog. Energ.* 43 (2018) 15191–15204.
- [82] F. Wang, S. He, H. Chen, B. Wang, L. Zheng, M. Wei, D.G. Evans, X. Duan, Active site dependent reaction mechanism over Ru/CeO₂ catalyst toward CO₂ methanation, *J. Am. Chem. Soc.* 138 (2016) 6298–6305.
- [83] P. Hongmanorom, J. Ashok, P. Chirawatkul, S. Kawi, Interfacial synergistic catalysis over Ni nanoparticles encapsulated in mesoporous ceria for CO₂ methanation, *Appl. Catal., B* 297 (2021), 120454.
- [84] P.H. Ho, G.S. de Luna, S. Angelucci, A. Canciani, W. Jones, D. Decarolis, F. Ospitali, E.R. Aguado, E. Rodríguez-Castellón, G. Fornasari, A. Vaccari, A.M. Beale, P. Benito, Understanding structure-activity relationships in highly active La promoted Ni catalysts for CO₂ methanation, *Appl. Catal., B* 278 (2020), 119256.
- [85] H.L. Huynh, J. Zhu, G. Zhang, Y. Shen, W.M. Tucho, Y. Ding, Z. Yu, Promoting effect of Fe on supported Ni catalysts in CO₂ methanation by in situ DRIFTS and DFT study, *J. Catal.* 392 (2020) 266–277.
- [86] X. Su, X. Yang, Y. Huang, B. Liu, T. Zhang, Single-atom catalysis toward efficient CO₂ conversion to CO and formate products, *Acc. Chem. Res.* 52 (2019) 656–664.